Monthly Notices
of the
ROYAL ASTRONOMICAL SOCIETY

Mon. Not. R. Astron. Soc. **427,** 550–568 (2012) doi:10.1111/j.1365-2966.2012.21984.x

Evidence for significant growth in the stellar mass of brightest cluster galaxies over the past 10 billion years

C. Lidman,[1⋆] J. Suherli,[1,2] A. Muzzin,[3] G. Wilson,[4] R. Demarco,[5] S. Brough,[1] A. Rettura,[4] J. Cox,[4] A. DeGroot,[4] H. K. C. Yee,[6] D. Gilbank,[7] H. Hoekstra,[3] M. Balogh,[8] E. Ellingson,[9] A. Hicks,[10] J. Nantais,[5] A. Noble,[11] M. Lacy,[12] J. Surace[13] and T. Webb[10]

[1]*Australian Astronomical Observatory, PO Box 296, Epping, NSW 1710, Australia*
[2]*Bosscha Observatory, Institut Teknologi Bandung, Lembang, Bandung, West Java, Indonesia*
[3]*Leiden Observatory, Leiden University, PO Box 9513, 2300 RA Leiden, the Netherlands*
[4]*Department of Physics and Astronomy, University of California, Riverside, CA 92521, USA*
[5]*Department of Astronomy, Universidad de Concepcion, Casilla 160-C, Concepcion, Chile*
[6]*Department of Astronomy & Astrophysics, University of Toronto, 50 St George Street, Toronto, Ontario M5S 3H4, Canada*
[7]*South African Astronomical Observatory, PO Box 9, Observatory 7935, South Africa*
[8]*Department of Physics and Astronomy, University of Waterloo, Waterloo, Ontario N2L 3G1, Canada*
[9]*Center for Astrophysics and Space Astronomy, 389UCB, University of Colorado, Boulder, CO 80309, USA*
[10]*Department of Physics and Astronomy, Michigan State University, East Lansing, MI 48824-2320, USA*
[11]*Department of Physics, McGill University, Montreal, QC H3A 0G4, Canada*
[12]*North American ALMA Science Center, NRAO Headquarters, 520 Edgemont Road, Charlottesville, VA 22903, USA*
[13]*Spitzer Science Center, California Institute of Technology, 220-6, Pasadena, CA 91125, USA*

Accepted 2012 August 23. Received 2012 August 23; in original form 2012 July 6

ABSTRACT

Using new and published data, we construct a sample of 160 brightest cluster galaxies (BCGs) spanning the redshift interval $0.03 < z < 1.63$. We use this sample, which covers 70 per cent of the history of the universe, to measure the growth in the stellar mass of BCGs after correcting for the correlation between the stellar mass of the BCG and the mass of the cluster in which it lives. We find that the stellar mass of BCGs increases by a factor of 1.8 ± 0.3 between $z = 0.9$ and $z = 0.2$. Compared to earlier works, our result is closer to the predictions of semi-analytic models. However, BCGs at $z = 0.9$, relative to BCGs at $z = 0.2$, are still a factor of 1.5 more massive than the predictions of these models. Star formation rates in BCGs at $z \sim 1$ are generally too low to result in significant amounts of mass. Instead, it is likely that most of the mass build up occurs through mainly dry mergers in which perhaps half of the mass is lost to the intra-cluster medium of the cluster.

Key words: galaxies: clusters: general – galaxies: evolution – galaxies: high-redshift – cosmology: observations.

1 INTRODUCTION

Brightest cluster galaxies (BCGs) are amongst the largest, most luminous and most massive galaxies in the universe at the present epoch. Located in the cores of rich galaxy clusters, BCGs are easy to identify, both observationally and in simulations. They can also be observed at a time when the universe was less than a third of its current age. They therefore provide an attractive target for testing our understanding of the processes that drive galaxy evolution, albeit in the most massive galaxies of the universe.

In the hierarchical scenario for the formation of structure in our universe, galaxies start off as small fluctuations in the density of matter and build up their stellar mass over time by converting material accreted from their surroundings into stars and by merging with other galaxies (see Baugh 2006, for a review). In semi-analytic models that use the hierarchical scenario as their foundation, the stellar mass of a BCG increases significantly with time. For example, between redshift $z = 1.0$ (corresponding to a look-back time of 6.7 Gyr) and $z = 0$, the semi-analytic model described in De Lucia & Blaizot (2007) predicts that BCGs increase their stellar mass by a factor of 4.

In contrast to this prediction, observations appear to suggest that there is little growth in the stellar mass of BCGs, although apparently

⋆E-mail: clidman@aao.gov.au

© 2012 The Authors
Monthly Notices of the Royal Astronomical Society © 2012 RAS

Table 1. Observational summary.

Cluster	Redshift	RA[5] J2000	Dec.[5] J2000	Instrument/Telescope	Exposure times: J and K_s (s)	(s)
SpARCS J003442−430752 [1]	0.867	00:34:42.03	−43:07:53.4	ISPI/Blanco	17 280	8800
SpARCS J003645−441050 [1]	0.869	00:36:44.99	−44:10:49.8	ISPI/Blanco	17 280	7080
SpARCS J161314+564930 [1,2]	0.871	16:13:14.63	56:49:30.0	WIRCAM/CFHT	6240	6300
SpARCS J104737+574137 [1]	0.956	10:47:33.43	57:41:13.4	WIRCAM/CFHT	7560	2400
SpARCS J021524−034331 [1]	1.004	02:15:23.99	−03:43:32.2	ISPI/Blanco	26 640	11 800
SpARCS J105111+581803 [1]	1.035	10:51:11.22	58:18:03.3	WIRCAM/CFHT	6840	2700
SpARCS J161641+554513 [1,2]	1.156	16:16:41.32	55:45:12.4	WIRCAM/CFHT	18 960	7000
SpARCS J163435+402151 [1,3]	1.177	16:34:38.21	40:20:58.4	WIRCAM/CFHT	11 640	6850
SpARCS J163852+403843 [1,3]	1.196	16:38:51.64	40:38:42.8	WIRCAM/CFHT	11 640	6000
SpARCS J003550−431224 [1,4]	1.335	00:35:49.68	−43:12:23.8	HAWK-I/Yepun	11 040	12 000
Cluster	Redshift	RA[5] J2000	Dec.[5] J2000	Instrument/Telescope	Exposure times: Y and K_s (s)	(s)
SpARCS J033056−284300	1.626	03:30:55.87	−28:42:59.7	HAWK-I/Yepun	8880	3040
SpARCS J022426−032331	1.633	02:24:26.32	−03:23:30.7	HAWK-I/Yepun	8640	5040

Notes. 1. Muzzin et al. (2012); 2. Demarco et al. (2010); 3. Muzzin et al. (2009); 4. Wilson et al. (2009); 5. Coordinates of the BCG.

conflicting results have been reported. Using a sample of optically selected clusters, Aragon-Salamanca, Baugh & Kauffmann (1998) found that the stellar mass of BCGs grew by a factor of 4 between $z = 1$ and today. Burke, Collins & Mann (2000), on the other hand, using a sample of X-ray selected clusters over a similar redshift range, find substantially less growth.[1] Burke et al. (2000) conclude that sample selection can explain part of the difference between their results and those in Aragon-Salamanca et al. (1998), a conclusion that was supported by Nelson et al. (2002). In an independent study, using an optically selected sample of 21 high-redshift clusters, Whiley et al. (2008) find little change in the stellar mass of BCGs since $z \sim 1$.

At higher redshifts, the discrepancy between the models and the observations is larger. Collins et al. (2009) and Stott et al. (2010), using a sample of 20 mostly X-ray selected clusters and a sample of nearby clusters from Stott et al. (2008), find that there is little growth between $z \sim 1.4$ and now. At $z \sim 1.4$, the semi-analytic model of De Lucia & Blaizot (2007) predicts that BCGs should be a factor of 6 less massive. Therefore, there appears to be clear disagreement between the models and the observations.

In this paper, we expand upon the work that has been done so far in three ways. First, we increase the number of BCGs beyond $z = 0.8$ for which accurate near-IR (NIR) photometry is available. Secondly, we extend the redshift baseline by including the BCGs in two recently discovered clusters at $z \sim 1.6$. Thirdly, we use our large sample to account for the correlation between the stellar mass of the BCG and the mass of the cluster in which it lives.

We start the paper with a description of our new sample of BCGs in Section 2, followed, in Section 3, by a description of the NIR imaging data that we use in later sections. In Sections 4 and 5, we derive the magnitudes and colours of the BCGs in our sample and compare them to predictions made by simple and composite stellar population models. Following Stott et al. (2010), we use this comparison to estimate stellar masses. In Section 6, we discuss our results, comparing them to the predictions made by semi-analytic models and examining how robust they are to our methods. In the final section, we summarize our main results. Throughout the paper, all magnitudes and colours are measured in the observer frame and are placed on the Two-Micron All-Sky Survey (2MASS) photometric system. Vega magnitudes are used throughout the paper. We also assume a flat cold dark matter cosmology with $\Omega_\Lambda = 0.73$ and $H_0 = 70\ \mathrm{km\ s^{-1}\ Mpc^{-1}}$.

2 A NEW SAMPLE OF DISTANT BCGs

We use clusters from the SpARCS[2] survey (Muzzin et al. 2009, 2012; Wilson et al. 2009; Demarco et al. 2010) to assemble a sample of 12 BCGs spanning the redshift interval $0.85 < z < 1.63$. The coordinates and redshifts of the clusters are listed in Table 1. Ten of the 12 clusters were observed in the GCLASS[3] survey, which used the Gemini Multi-object Spectrographs on Gemini North and Gemini South Telescopes to obtain between 20 and 80 spectroscopically confirmed members per cluster (Muzzin et al. 2012). The other two clusters, which are the most distant clusters in our sample, are more recent discoveries. Both clusters are spectroscopically confirmed, with a dozen spectroscopic redshifts per cluster (Muzzin et al., in preparation; Wilson et al., in preparation).

All 12 clusters were discovered by searching for over-densities in the number of red galaxies using a combination of images taken with the Infrared Array Camera (IRAC) on the *Spitzer Space Telescope* with z-band images taken with either MegaCam on the Canada–France–Hawaii Telescope (CFHT) or MOSAIC II on the Cerro Tololo Blanco Telescope. The 10 GCLASS clusters were found using the z-[3.6] colour, whereas the two more distant clusters were found using the [3.6]-[4.5] colour together with the requirement of a red z-[3.6] colour. Further details on how the clusters were discovered can be found in Muzzin et al. (2008, 2009, in preparation) and Wilson et al. (2009).

[1] Both Aragon-Salamanca et al. (1998) and Burke et al. (2000) use an Einstein–de-Sitter universe, i.e. $\Omega_M, \Omega_\Lambda = 1, 0$, with $H_0 = 50\ \mathrm{km\ s^{-1}\ Mpc^{-1}}$ for the cosmology. While their results are not directly comparable to the results in later papers, one can compare the results of the two papers.

[2] Spitzer Adaptation of the Red-Sequence Cluster Survey, www.faculty.ucr.edu/∼gillianw/SpARCS/

[3] Gemini Cluster Astrophysics Spectroscopic Survey, www.faculty.ucr.edu/∼gillianw/GCLASS/

Table 2. Instrument summary.

Instrument	Telescope	Pixel scale (arcsec)	FoV (arcmin)	Detector
WIRCAM[1]	CFHT	0.304	20.5	2 × 2 Hawaii-2RG mosaic
ISPI[2]	Blanco	0.307	10.3	Hawaii-2
HAWK-I[3]	Yepun (VLT-UT4)	0.1065	7.5	2 × 2 Hawaii-2RG mosaic

Notes. 1. Puget et al. (2004); 2. van der Bliek et al. (2004); 3. Pirard et al. (2004) and Casali et al. (2006).

3 OBSERVATIONS

We used three NIR imaging cameras to observe 12 clusters. Six of the clusters were observed with the Wide-field InfraRed Camera (WIRCam) on the CFHT on Mauna Kea. Another three clusters were imaged with the Infrared Side Port Imager (ISPI) on the Blanco Telescope at the Cerro Tololo Inter-American Observatory (CTIO). Finally, the three most distant clusters were imaged with the High Acuity Wide field K-band Imager (HAWK-I) on Yepun [Very Large Telescope Unit Telescope 4 (VLT-UT4)] at the European Southern Observatory (ESO) Cerro Paranal Observatory. The fields-of-view of the imagers and their plate scales are noted in Table 2. Details of the observations, including exposure times, are listed in Table 1. With the exception of the two most distant clusters (SpARCS J033056−284300 and SpARCS J022426−032331), all clusters were imaged in J and K_s. At the time SpARCS J033056−284300 and SpARCS J022426−032331 were observed with HAWK-I, neither cluster had been spectroscopically confirmed. The Y and K_s filter pair were chosen over J and K_s, since the former pair almost straddle the 4000 Å break, thereby increasing the contrast of cluster members over field galaxies and easing target selection for spectroscopy.

3.1 Data reduction

The processing of the raw data was done in a standard manner and largely follows the steps outlined in Lidman et al. (2008). Data from each of the cameras were pre-processed (dark subtraction, flat-fielding and sky subtraction) using a combination of observatory-developed instrument pipelines (e.g. the CFHT data were processed with version 1.0 of the 'I'iwi pipeline[4]) and our own scripts using IRAF.[5]

SCAMP (version 1.6.2) and SWARP (version 2.17.6)[6] were used to map the sky-subtracted images on to a common astrometric reference frame. After accounting for gain variations between chips (only relevant for the data that were taken with HAWK-I and WIRCAM) and creating individual bad pixel maps to account for bad pixels and remnants from bright stars observed in previous frames, the images were then combined with the `imcombine` task within IRAF. Each image was weighted with the inverse square of the full width at half-maximum of the point spread function.

With the exception of the data taken in the Y band, zero-points were set using stars from the 2MASS point-source catalogue (Skrutskie et al. 2006). Typically, between 10 and 40 unsaturated 2MASS stars with 2MASS quality flags of 'A' or 'B' were selected to measure zero-points and their uncertainties. 2MASS stars were weighted by the reported uncertainties in the 2MASS point-source catalogue. The uncertainties in the zero-points are generally less than 2 per cent, and more typically 1 per cent, for both J and K_s. For Y, the zero-point was set using standard stars that were observed during the same night as the clusters. The uncertainty is estimated from the night-to-night variation in the zero-points and is around 2 per cent.

3.2 Data quality

Overall, the depth and quality of the imaging data vary substantially from one image to another. The image quality, as measured from bright stars, varies from 0.3 arcsec in the data taken with HAWK-I to 1.5 arcsec in the data taken with ISPI.

The image depth, which we define as the 5σ point-source detection limit, varies from 19.5 for the K_s-band image of SpARCS J003645−441050 to 25.1 for the Y-band image of SpARCS J022426−032331. In all cases, the BCG is at least 2 mag brighter than the detection limit. The median signal-to-noise ratio is around 50. Table 3 summarizes the image quality and image depth.

4 ANALYSIS

Identifying the brightest galaxy[7] in each cluster was generally straightforward. Images of the BCGs are shown in Fig. 1, and their coordinates are listed in Table 1. With only two exceptions – SpARCS J105111+581803 and SpARCS J163435+402151 – the BCGs are located near to the projected centre of the clusters. For both SpARCS J105111+581803 and SpARCS J163435+402151, the BCGs are ∼250 kpc from the projected centre of the cluster. The projected distances are not excessively large when compared to low-redshift clusters (Bildfell et al. 2008; Sehgal et al. 2012), and both BCGs have redshifts that place them within 300 km s^{-1} of cluster redshift.

4.1 Photometry

To estimate total magnitudes of the BCGs in the SpARCS clusters, we follow Stott et al. (2010) and use the SExtractor[8] `MAG_AUTO` magnitude. `MAG_AUTO` is a Kron-like magnitude (Kron 1980) within an elliptical aperture. For a given object, the elongation and orientation of the aperture are determined by second-order moments of the light distribution. In this paper, the size of the aperture is set to the standard value of 2.5 times the first raw moment. Note that the definition of the first raw moment used by SExtractor differs from the one used in Kron (1980). See the SExtractor user's manual and

[4] http://www.cfht.hawaii.edu/Instruments/Imaging/WIRCam/

[5] IRAF is distributed by the National Optical Astronomy Observatories which are operated by the Association of Universities for Research in Astronomy, Inc., under the cooperative agreement with the National Science Foundation.

[6] http://www.astromatic.net/

[7] Throughout this paper, the BCG is defined as the brightest cluster member in the observer-frame K_s band.

[8] We used version 2.6.6 of SExtractor – http://www.astromatic.net/ – in double image mode.

Table 3. Image quality and image depth.

Cluster	Image quality (arcsec)	Image depth[a] (mag)	Image quality (arcsec)	Image depth[a] (mag)
	J		K_s	
SpARCS J003442−430752	1.25	21.8	0.98	19.9
SpARCS J003645−441050	1.13	21.7	1.47	19.5
SpARCS J161314+564930	0.77	22.2	0.72	21.1
SpARCS J104737+574137	0.69	22.2	0.60	21.2
SpARCS J021524−034331	1.07	21.8	0.89	20.3
SpARCS J105111+581803	0.66	22.5	0.74	20.6
SpARCS J161641+554513	0.70	22.8	0.75	21.2
SpARCS J163435+402151	0.65	22.9	0.67	21.2
SpARCS J163852+403843	0.61	23.1	0.58	21.5
SpARCS J003550−431224	0.35	24.6	0.31	23.1
	Y		K_s	
SpARCS J033056−284300	0.45	24.0	0.29	21.9
SpARCS J022426−032331	0.34	25.1	0.51	21.5

[a]The image depth is the 5σ point-source detection limit measured over an aperture that has a diameter that is twice the image quality.

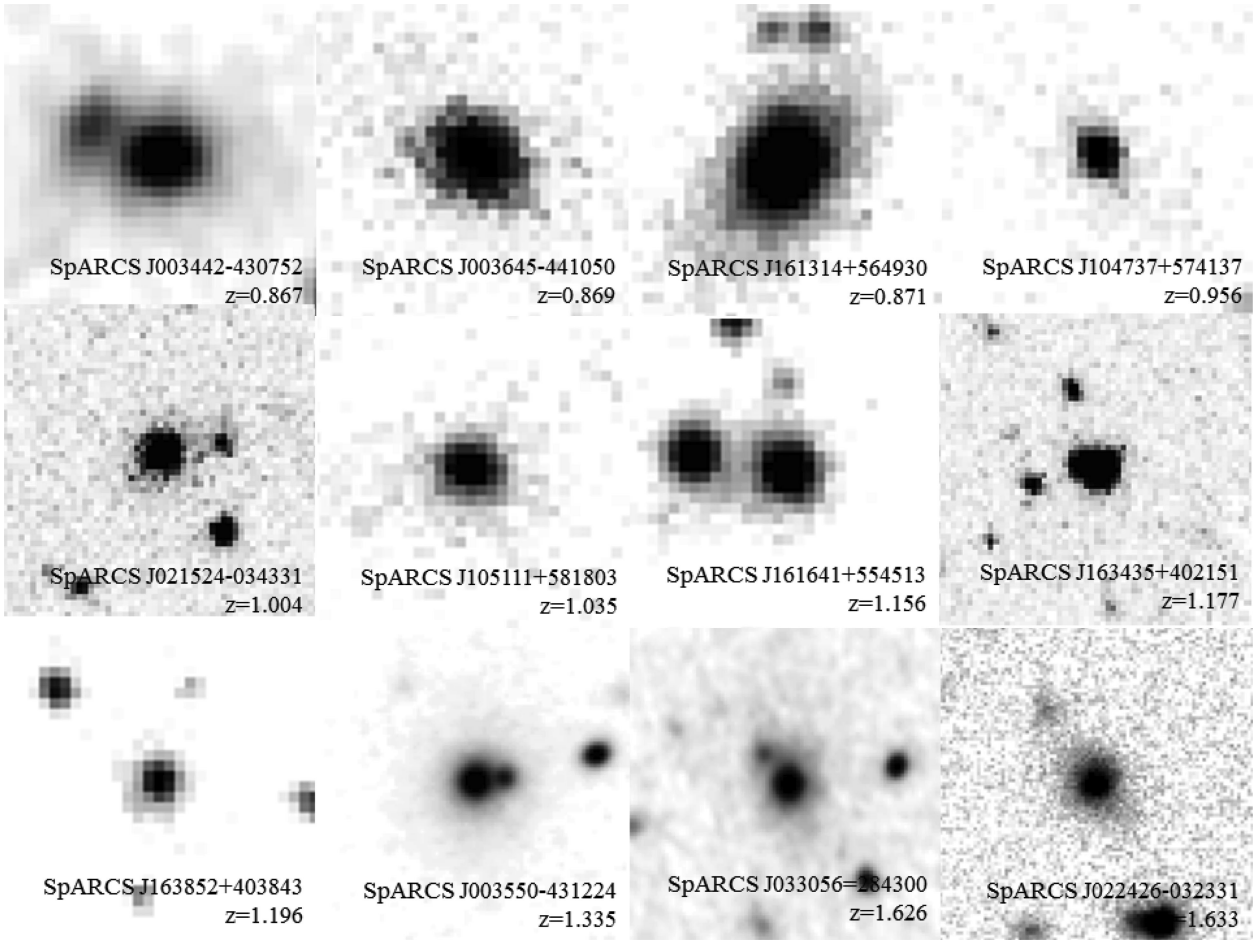

Figure 1. K_s-band cutouts of the 12 BCGs used in this paper. The images are 9 arcsec on a side, which corresponds to 70 kpc for the nearest BCG and 78 kpc for the most distant.

Graham & Driver (2005) for further details. Other SExtractor parameters are set to their default values. For example, the background is determined globally and the minimum Kron radius is set to 3.5, the units of which are not pixels but in units of the semi-major (or semi-minor) axis.

For measuring colours, we first match the image quality between images using the IRAF `psfmatch` task and then measure the flux in apertures that have a diameter of 16 kpc. We use the same physical diameter for all BCGs. At $z \sim 1$, this projects to ∼2.1 arcsec on the sky. The apertures we use are double the size of the apertures used

© 2012 The Authors, MNRAS **427,** 550–568
Monthly Notices of the Royal Astronomical Society © 2012 RAS

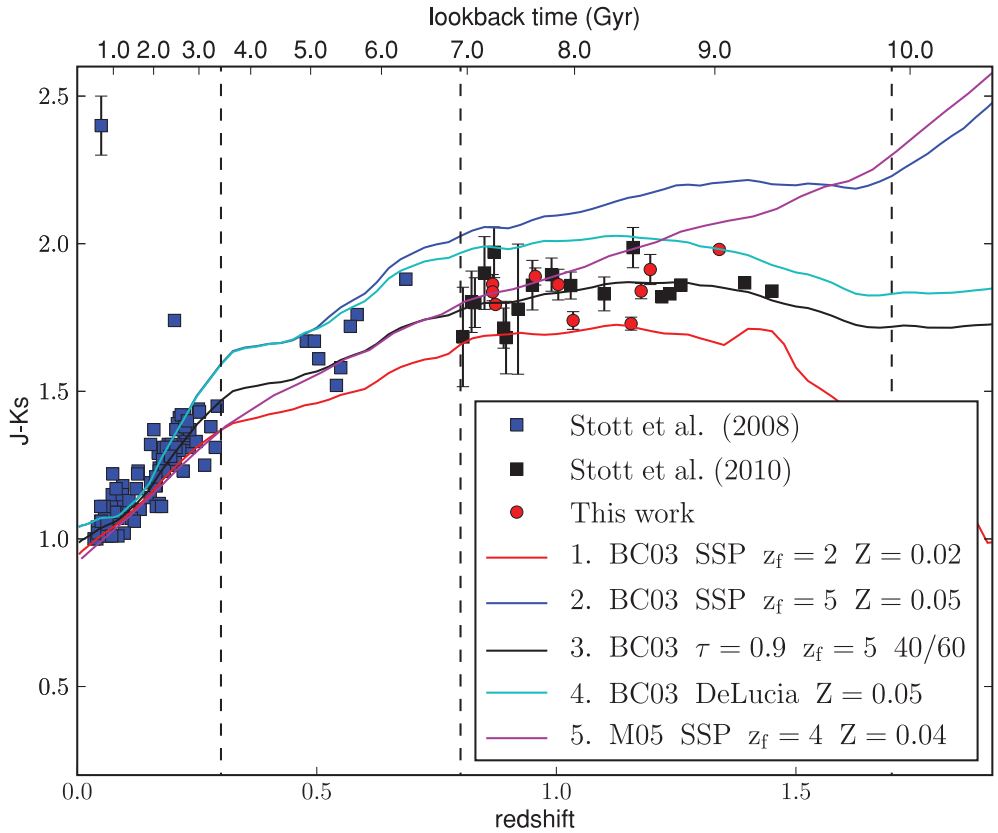

Figure 2. The observer-frame $J - K_s$ colour of BCGs in our sample as a function of redshift. The data from this paper are plotted as red circles. The two most distant clusters and clusters from the CNOC1 sample are not plotted as they lack J-band data. The vertical dashed lines mark the boundaries of the low-, intermediate- and high-redshift subsamples that are described in the text. The evolution in the $J - K_s$ colour for several stellar population models is plotted as the continuous lines. A broad range of models is shown. Note how well our best-fitting model, model 3, which is the model we use to estimate stellar masses, describes the change in $J - K_s$ colour with redshift. See text and Table 6 for additional details.

in Stott et al. (2010). The image quality of the poorest images – the K_s-band image of SpARCS J003645−441050, for example – is not sufficiently good enough to use apertures this small.

We investigated how the colours change with the size of the apertures. We varied the aperture diameter from 10 to 24 kpc. With three exceptions, the colours change by less than 2 per cent, which is similar to the statistical uncertainty. The exceptions are the BCGs in SpARCS J105111+581803 and our two most distant clusters, where we see changes of up to 6 per cent. Interestingly, the BCG of SpARCS J105111+581803 is about 250 kpc from the centre of the cluster, is an [O II] emitter and has, relative to other BCGs, a blue colour. Our two most distant BCGs, which were observed in Y and K_s, are also [O II] emitters. The change in colour with aperture diameter might indicate that these galaxies have substantial colour gradients. The other BCGs do not show any evidence for colour gradients over the range of apertures explored.

Errors in the photometry are dominated by sky noise, so they were estimated by examining the distribution of the integrated counts in apertures that were randomly placed in regions that were free of objects. For colours, the errors were estimated for each filter separately and then added in quadrature.

The filter transmission curves of the J and K_s bands in ISPI, WIRCam and HAWK-I are similar to one another, however, they differ slightly from the filter curves of the respective filters used in 2MASS. To account for this difference we offset the colours by an amount that depends on (i) the average spectral energy distribution (SED) of the stars used to determine the image zero-points, (ii) the SED of the BCG and (iii) its redshift. To determine the offset, we assume that the average star can be modelled as a K5 dwarf, which has a $J - K_s$ colour that is similar to the average colour of stars that are used to determine the zero-point, and that the SED of the BCG corresponds to the one predicted by model 3 in Fig. 2 (see Section 5.2 for a detailed description of this model). Between redshifts 0.8 and 1.6, the magnitude of the correction is about 0.08 mag. At these redshifts, the dependence of the correction on redshift and the assumed spectrum of the BCG is slight, with extreme values differing by 0.03 mag.

The magnitudes and colours of the 12 BCGs in our sample are shown in Table 4.

4.2 External samples

To our sample of 12 high-redshift BCGs, we add BCGs from a number of external samples. At low to intermediate redshifts ($z = 0.04$ to $z = 0.83$), we add 103 of the 104 BCGs from Stott et al. (2008), excluding the BCG of MS1054.5−0321. At higher redshifts ($z = 0.81$ to $z = 1.46$), we use a sample of 20 BCGs from Stott et al. (2010). The BCG of MS1054.5−0321 is common to both samples. Like the 12 BCGs in our sample, the BCGs from these two external samples were observed in J and K_s.

For the $z < 0.15$ BCGs in Stott et al. (2008), the authors used photometry from the extended and point-source catalogues of 2MASS (Skrutskie et al. 2006). For the $z > 0.15$ BCGs, Stott et al. (2008) used the SExtractor `MAG_BEST` magnitude. Depending on the level

Table 4. SpARCS BCG photometry.

Cluster	Redshift	K_s (mag)	$J-K_s$ (mag)
SpARCS J003442−430752	0.867	16.516 (0.039)	1.863 (0.033)
SpARCS J003645−441050	0.867	16.092 (0.047)	1.837 (0.030)
SpARCS J161314+564930	0.873	15.693 (0.015)	1.794 (0.012)
SpARCS J104737+574137	0.956	17.140 (0.031)	1.889 (0.029)
SpARCS J021524−034331	1.004	16.876 (0.140)	1.861 (0.052)
SpARCS J105111+581803	1.035	16.877 (0.046)	1.740 (0.030)
SpARCS J161641+554513	1.156	17.017 (0.031)	1.729 (0.022)
SpARCS J163435+402151	1.177	17.349 (0.023)	1.839 (0.026)
SpARCS J163852+403843	1.196	17.647 (0.052)	1.913 (0.051)
SpARCS J003550−431224	1.340	17.524 (0.014)	1.981 (0.009)
SpARCS J033056−284300	1.620	17.881 (0.041)	... (...)
SpARCS J022426−032331	1.630	18.071 (0.026)	... (...)

Table 5. CNOC1 BCG photometry.

Cluster	Redshift	K_s (mag)
A2390	0.228	13.489 (0.068)
MS0440+02	0.197	13.337 (0.054)
MS0451+02	0.201	13.938 (0.065)
MS0839+29	0.193	13.411 (0.062)
MS1006+12	0.261	13.786 (0.074)
MS1231+15	0.235	13.891 (0.065)
MS1455+22	0.257	13.558 (0.062)
MS0016+16	0.547	15.288 (0.078)
MS0302+16	0.425	15.008 (0.065)
MS0451−03	0.539	15.176 (0.071)
MS1008−12	0.306	13.676 (0.076)
MS1224+20	0.326	14.409 (0.078)
MS1358+62	0.329	14.292 (0.063)
MS1512+36	0.373	14.632 (0.082)
MS1621+26	0.427	14.977 (0.069)

of crowding, `MAG_BEST` is either a corrected isophotal magnitude `MAG_ISOCOR` or the `MAG_AUTO` magnitude (Bertin & Arnouts 1996).

The BCGs in the high-redshift sample of Stott et al. (2010) are hosted by clusters that come from a number of sources. Not all of the clusters are X-ray selected; however, all are X-ray luminous, with X-ray luminosities exceeding 10^{44} erg s^{-1}. The photometry of these BCGs is measured with the SExtractor `MAG_AUTO` magnitude. The BCGs in the low-to-intermediate-redshift sample of Stott et al. (2008) are all hosted by clusters that have X-ray luminosities in excess of 10^{44} erg s^{-1} (in the 0.1–2.4 KeV band).

Additional BCG samples have been published in the literature. Aragon-Salamanca et al. (1998) published k-corrected K-band magnitudes for BCGs in 25 clusters up to $z = 0.92$. Whiley et al. (2008) combined this sample with 2MASS photometry of the low-redshift BCG sample of von der Linden et al. (2007) and their own photometry of a sample of 21 intermediate-to-high redshift ($0.39 < z < 0.96$) BCGs from the ESO Distant Cluster Survey. The photometry of all these samples is measured in fixed 37 kpc diameter apertures, and is converted to the rest-frame K band using k-corrections. In this paper, as in the papers of Stott et al. (2008, 2010), we do not apply k-corrections, and we measure the flux in differently sized apertures. These differences mean that we cannot use the photometry from these studies directly without inverting the k-corrections and applying a correction for the different size of the apertures. Without reanalysing the data, the latter is difficult to estimate, so we do not add the BCGs from these samples to ours.

In addition to the BCGs in Stott et al. (2010), we add BCGs in 15 X-ray luminous clusters from the intermediate-redshift CNOC1[9] cluster sample (Yee, Ellingson & Carlberg 1996). The CNOC1 clusters are from the Einstein Medium Sensitivity Survey (Gioia et al. 1990). We use the K_s-band photometry from Muzzin et al. (2007a); we note that these clusters were not observed in the J band.

K_s-band imaging data for 14 of the 15 CNOC1 clusters were obtained using the Ohio State-NOAO Infrared Imaging Spectrograph (ONIS) on the Kitt Peak National Observatory (KPNO) 2.1-m telescope. ONIS has a pixel scale of 0.288 arcsec, which is similar to the pixel scale of the cameras used to observe most of the clusters in our SpARCS sample. One cluster, MS 0440+02, was obtained using the PISCES camera on the Steward Observatory 90 inch (2.3 m) telescope. PISCES has a pixel scale of 0.495 arcsec. The image quality in the fully reduced images varies between 0.7 and 1.3 arcsec (See Muzzin et al. 2007a, for further details).

We have reanalysed the processed K_s-band images of clusters in the CNOC1 sample following the procedure used for clusters in our SpARCS sample (see Section 4.1). The K_s-band magnitude of these galaxies is reported in Table 5.

The BCGs from the four samples [SpARCS, CNOC1, Stott et al. (2008) and Stott et al. (2010)] are combined into a single sample that is then used to make three subsamples covering three broad redshift ranges: a low-redshift subsample ($0.0 < z \leq 0.3$), an intermediate-redshift subsample ($0.3 < z \leq 0.8$) and a high-redshift subsample ($0.8 < z < 1.65$). The number of BCGs in each of these subsamples is listed in Table 7. We use these subsamples throughout the rest of this paper.

5 ESTIMATING THE STELLAR MASS

Following the methods used in previous works on determining the stellar mass of BCGs (Stott et al. 2008, 2010; Collins et al. 2009), we use the offset between the observed and predicted observer-frame K_s-band magnitudes to estimate stellar mass. The predicted magnitude is estimated from stellar population models that match the observer-frame $J - K_s$ colour of the BCGs over the entire redshift range covered by our subsamples, i.e. from $z \sim 0$ to $z \sim 1.6$. When converting between luminosity and stellar mass we assume that the mass-to-light ratios of the BCGs are independent of stellar mass.

5.1 Modelling the $J - K_s$ colour

We use the simple stellar population (SSP) models from Bruzual & Charlot (2003, hereafter BC03) to model the evolution of the SEDs with cosmic time. There are a number of ingredients that go into the models, such as the initial mass function (IMF), the age and duration of the starburst, the metallicity of the stars and dust extinction.

We assume a Chabrier IMF (Chabrier 2003). The difference in the resulting $J - K_s$ colour from using a different IMF (e.g. a Salpeter IMF; Salpeter 1955) is less than 0.02 mag over the entire redshift range covered by the observations. Similarly, the stellar mass ratio between BCGs at low and high redshift is relatively unaffected by our choice of the IMF. The stellar masses themselves, however,

[9] Canadian Network for Observational Cosmology.

Table 6. Model parameters.

Model	Description	Origin	IMF	Formation redshift (Gyr)	τ	Metallicity
1	Low-redshift burst	BC03[a]	Chabrier	2.0	0.0	0.02 (solar)
2	High-redshift burst	BC03	Chabrier	5.0	0.0	0.05
3	Best-fitting model	BC03	Chabrier	5.0	0.9	60/40 split between 0.02 and 0.05
4	DeLucia et al. (2007) model	BC03	Chabrier	10.6	1.34	0.02
5	High-redshift burst	M05[b]	Salpeter	4.0	0.0	0.04

[a]BC03.
[b]M05.

change significantly. Excluding stellar remnants, the difference is about a factor of 2 for a given K_s-band luminosity. In this paper, we do not use the stellar masses directly, just their ratios.

We assume that extinction from dust in negligible. From the small amount of scatter in the colour of galaxies on the red-sequence, one can infer that dust either reddens all galaxies by a small amount or reddens a small number of galaxies considerably (Meyers et al. 2012). If the former is true, then the amount of reddening affecting the BCGs in our sample is unimportant. If the latter is true, then we would expect to see significant colour outliers in Fig. 2, which we do not see.

With the IMF set and dust ignored, we consider a series of models in which we allow the star formation history to vary. We add an extra dimension to these models by combining two models with identical star formation histories but different metallicities: a solar metallicity model and a model that is two-and-a-half times solar. At low redshifts ($z \sim 0.03$), BCGs have metallicities that are around twice solar (Loubser et al. 2009). We add this extra degree of freedom because it is not possible to match the colours of the BCGs over the entire redshift range – even by varying the star formation history – with the range of metallicities available in BC03. We allow the mass ratio of the two components to vary over the full range (i.e. 0.0 to 1.0) in steps of 0.1. We also allow the e-folding time, τ, of the star formation rate to vary between 0.3 and 1.0 Gyr in steps of 0.1 Gy. We then choose the model that best fits the data by finding the model with the smallest chi-square. With the exception of the CNOC1 sample and the two most distant clusters in the SpARCS sample, which lack J-band data, we use the entire sample when fitting the models. If an error in the $J - K_s$ colour is unavailable, we assume an error of 0.1 mag.

The best-fitting model, model 3 in Fig. 2, has an e-folding time of $\tau = 0.9$ Gyr and a composition that is split 60/40 between solar metallicity and a metallicity that is two-and-a-half times higher. This model accurately describes the general change in $J - K_s$ colour with redshift although it does not capture the scatter. In the remainder of this paper we use this model to estimate stellar masses.

In order to demonstrate the sensitivity of the $J - K_s$ colour on metallicity and different star formation histories, we plot a series of models. The parameters defining the models are listed Table 6. In model 1, all the stars form in a single burst at $z = 2$. In this model, all the stars have solar metallicity. Model 2 is similar to model 1, except that we move the burst to $z = 5$ and increase the metallicity to two-and-a-half times solar. In model 4, we move away from a single burst, using instead an exponentially decaying burst of star formation with $\tau = 1.03$ Gyr that starts forming stars at $z = 10.6$. This model mimics the star formation history of BCGs in the hierarchical models of De Lucia & Blaizot (2007), in which 50 per cent of the stellar mass is formed by $z = 5$ and 80 per cent by $z = 3$. Our fifth model is a model from Maraston (2005, hereafter M05). We will discuss this model further in Section 6, where we will use this model to test how sensitive out results are to our choice of stellar evolution models.

5.2 Evolution in the stellar mass of BCGs

In Fig. 3, we plot the observer-frame K_s-band magnitudes of the BCGs in our sample against their redshifts. BCGs from Stott et al. (2008, 2010) are plotted as the blue and black squares, respectively, while BCGs in the SpARCS and CNOC1 clusters are plotted as red circles. While the red circles generally land within the area covered by the squares, the CNOC1 and SpARCS BCGs are less dispersed with respect to the models than the BCGs in Stott et al. (2008).

Furthermore, the BCGs in the SpARCS clusters appear to be slightly brighter than the other BCGs in the high-redshift subsample, although this difference seems to be largely driven by a few BCGs at $z \sim 0.9$. The clusters hosting the SpARCS BCGs and the other clusters in the high-redshift subsample have similar masses, so the correlation between cluster mass and the BCG stellar mass (see Section 5.3) is not the cause for the difference. Clusters in SpARCS were selected as galaxy overdensities, whereas most of the other clusters were selected through their X-ray emission. It is tempting to speculate that the difference is caused by the way the clusters were selected. However, the high-redshift sample is small, and we believe that a larger independent sample is required before one could conclusively state that sample selection is the reason for the difference.

In addition to the individual BCGs, we also plot the predictions of the models described in the previous section. The normalization[10] of the models is constrained by the data in the low-redshift subsample. With this normalization, the BCGs at low redshift correspond to galaxies that are about 2 mag brighter than a L_* galaxy in the Coma cluster (de Propris et al. 1998).

The stellar mass of individual galaxies is derived by converting the offset in magnitude between model 3, the model that best describes the evolution in the $J - K_s$ colour with redshift, and the observed K_s-band magnitude to a stellar mass. We normalize the stellar mass of the BCGs to the stellar mass they would have by today, using the modelled decrease in stellar mass with time from stellar winds and supernova explosions (BC03). The results for the model that best follows the general evolution in the $J - K_s$ colour, model 3, are shown in Table 7. In the last column of this table, we also list the median stellar mass of the BCGs at the cluster redshift.

[10] The normalization is computed by matching the magnitude of the models at the median redshift of the low-redshift subsample with the median magnitude of the low-redshift subsample. It differs from the normalization adopted in Collins et al. (2009) and Stott et al. (2010). In these studies the normalization occurs over a more restrictive redshift interval ($z < 0.05$). See Section 6.3 for further details.

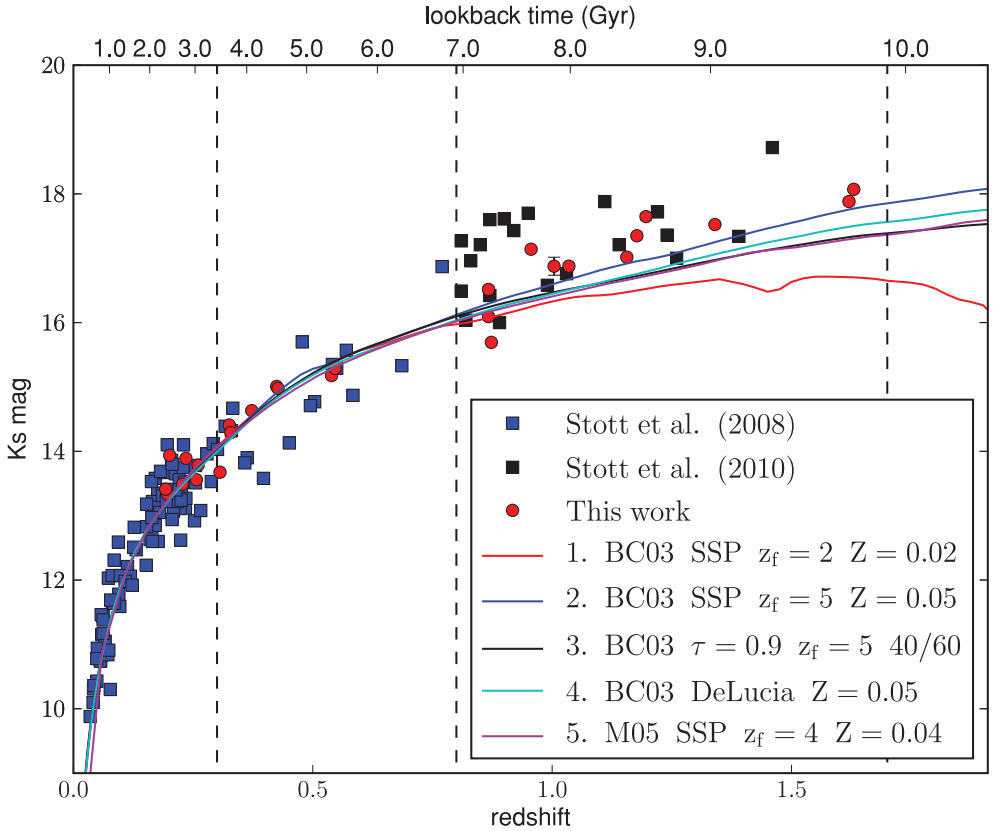

Figure 3. The observer-frame K_s-band magnitude of BCGs as a function of redshift. The data from this paper are plotted as the red circles. Red circles beyond $z \sim 0.8$ are BCGs in the SpARCS clusters, while those below $z \sim 0.8$ are BCGs in the CNOC1 clusters. The vertical dashed lines mark the boundaries of the low-, intermediate- and high-redshift subsamples that are described in the text. The predicted K_s magnitudes of the models plotted in Fig. 2 and listed in Table 6 are shown as the continuous lines. The models are normalized to the data in the low-redshift bin. They are discussed in Section 5.2. Note how all models tend to underpredict the flux in high-redshift BCGs.

Table 7. The three subsamples described in Section 4.2 and the SpARCS sample. For all quantities, we report the median value.

Subsample	Redshift range	Size	Redshift	Cluster mass[a] (10^{15} $M_\odot$)	Cluster mass[b] (10^{15} $M_\odot$)	BCG mass[c] (10^{12} $M_\odot$)	BCG mass[d] (10^{12} $M_\odot$)
Low	$z \leq 0.3$	93 (90)	0.17	0.79[e]	0.59[e]	0.45	0.46
Intermediate	$0.3 < z \leq 0.8$	25 (18)	0.45	2.34[e]	1.27[e]	0.50	0.52
High	$0.8 < z \leq 1.7$	32 (32)	1.00	1.20	0.30	0.29	0.32
SpARCS	$0.8 < z \leq 1.7$	12 (12)	1.10	1.19	0.29	0.31	0.34

[a]Cluster masses corrected for the growth they are likely to have by today.
[b]Cluster masses at the redshift of the cluster.
[c]The stellar mass of the BCG at redshift zero (accounts for stellar mass loss).
[d]The stellar mass of the BCG at the redshift of the cluster.
[e]Computed for the subset of clusters (numbered in brackets) with masses. See text for details.

When comparing the stellar mass of BCGs at low and high redshift we compare the stellar masses they would have by today – the second last column in this table.

Without making any correction for the positive correlation between the stellar mass of the BCG and the mass of cluster (see Edge 1991; Burke et al. 2000; Brough et al. 2008; Whiley et al. 2008, and the next section), the data indicate that the stellar mass of the BCGs increase by a factor of 1.55 ± 0.18 between $z \sim 1$ and $z \sim 0.17$. The errors are determined by bootstrap resampling. The increase is found for the high-redshift subsample as a whole and for a smaller subsample consisting of just the clusters from SpARCS. In the next section we examine how the correlation between the stellar mass of the BCG and the mass of cluster affects our results.

5.3 Accounting for cluster masses

The stellar mass of BCGs correlates with cluster mass in the sense that larger clusters tend to host larger BCGs (Edge 1991; Burke et al. 2000; Brough et al. 2008; Whiley et al. 2008; Stott et al. 2012). Comparing the stellar mass of BCGs in our three subsamples without accounting for this correlation will lead to biased results if the median mass of the clusters in the subsamples differs.

To account for this correlation, we first need to estimate how clusters grow in mass so that we can fairly compare clusters that are observed at different redshifts. Over the redshift range that our sample covers, clusters grow significantly. For example, in the hierarchical model of structure formation, a cluster with a mass of $5 \times 10^{14}\,M_{\odot}$ at $z = 1$ is predicted to grow by a factor of about 3 by today (Wechsler et al. 2002; Fakhouri, Ma & Boylan-Kolchin 2010). Fakhouri et al. (2010), who use the Millennium and Millennium II simulations (Springel et al. 2005; Boylan-Kolchin et al. 2009), and Wechsler et al. (2002), who use an independent simulation (Bullock et al. 2001), find similar growth rates. We use mean accretion rates in Fakhouri et al. (2010) to estimate the mass each cluster should have by the current epoch using the masses they had at the redshifts they were observed. We describe how we estimate cluster masses at the redshift at which they were observed in Section 5.3.1.

After evolving our clusters forward in time to today, we find that the median mass of the clusters in our three subsamples differs by as much as a factor of 3 (see Table 7). The differences in the subsamples reflect the volumes probed and sensitivity limits of the surveys that were used to build our subsamples. Since clusters in the intermediate- and high-redshift subsamples are, by the current epoch, more massive than those in the low-redshift subsample, the correlation between cluster mass and BCG stellar mass – if uncorrected – leads to an underestimate in the amount of evolution in the stellar mass of BCGs.

In this paper, we explore a couple of approaches to account for the correlation. In the first approach, we first match the cluster mass distributions in the samples being compared before comparing the masses of the BCGs. In the second approach, we normalize BCG stellar masses to some fiducial mass using the relationship between cluster mass and the BCG stellar mass.

Our approaches to account for this correlation differ from approaches used in the past. In Whiley et al. (2008), clusters are grouped according to the mass they had at the redshift they were observed. In Stott et al. (2010), the mass of BCGs is compared to the mass of BCGs from semi-analytic models after first matching the masses of the clusters in the semi-analytic models to the observed masses.

5.3.1 Estimating cluster mass

Given the heterogeneous nature of the data that are available for our clusters, we estimate cluster masses[11] in different ways. For clusters in the low- and intermediate-redshift subsamples of Stott et al. (2008), we use the M_{500} masses listed in Mantz et al. (2010). These masses are converted to M_{200} assuming that the cluster mass profile follows a Navarro–Frenk–White profile (Navarro, Frenk & White 1997) with a concentration index of 5. For the conversion, we use the formulae listed in appendix C of Hu & Kravtsov (2003). Only about a quarter of the clusters in Stott et al. (2008) are in Mantz et al. (2010). To increase the number of clusters in Stott et al. (2008) with mass measurements, we use the X-ray temperatures (Ebeling et al. 2007, 2010) and the X-ray luminosities (Ebeling et al. 1996, 1998, 2000) of these clusters (the luminosities were corrected for the cosmology used in this paper) and the temperature–mass and luminosity–mass relations in Mantz et al. (2010) to estimate cluster masses.

[11] We use M_{200} for cluster masses. M_{200} is the mass contained within a radius within which the mean density of the cluster exceeds the critical density of the Universe at the redshift of the cluster by a factor of 200.

21 of the clusters in Ebeling et al. (2007, 2010) and Mantz et al. (2010) are also in Ebeling et al. (1996, 1998, 2000), which enables us to compare the mass derived from the X-ray luminosity with the mass derived from X-ray temperature. The median ratio is 1.14 with an standard deviation (s.d.) of 0.53. We correct the masses determined from the X-ray luminosity by the median ratio and use the s.d. as a measure of the uncertainty in the conversion.

For the SpARCS clusters, we estimate the cluster mass from the line-of-sight velocity dispersion (Wilson et al., in preparation). For clusters in the high-redshift subsample of Stott et al. (2010), we use the X-ray temperature reported in that paper and convert them to masses using the relation in Mantz et al. (2010). For all but two of the clusters in the intermediate-redshift subsample of Muzzin et al. (2007a) we use the X-ray temperatures listed in Hicks et al. (2006) and convert them to masses using the relation in Mantz et al. (2010). For the remaining two clusters (MS1224+20 and MS1231+15), we use the masses listed in Muzzin et al. (2007b), which are computed from the line-of-sight velocity dispersion.

After removing clusters from Stott et al. (2008) that are not listed in Ebeling et al. (1996, 1998, 2000, 2007, 2010) and Mantz et al. (2010), we end up with 90 and 18 clusters in the low- and intermediate-redshift subsamples, respectively. The number of clusters in the high-redshift subsample is unchanged. The numbers are listed in Table 7. Altogether, there are 152 clusters in our three subsamples.

5.3.2 Cluster mass versus BCG stellar mass

The correlation between cluster mass (at the redshift at which it was observed) and BCG stellar mass for these three subsamples is shown in Fig. 4. Errors in the mass of the BCGs are derived from errors in the photometry. If an error in the K_s-band photometry was unavailable, we conservatively set the error to 10 per cent. Our results are not very sensitive to this value, as errors in the cluster masses are much larger. Errors in the mass of the clusters are discussed in Section 5.3.3. We note that clusters in the intermediate-redshift subsample generally have higher masses than clusters in the low-redshift subsample. As noted earlier, the difference between

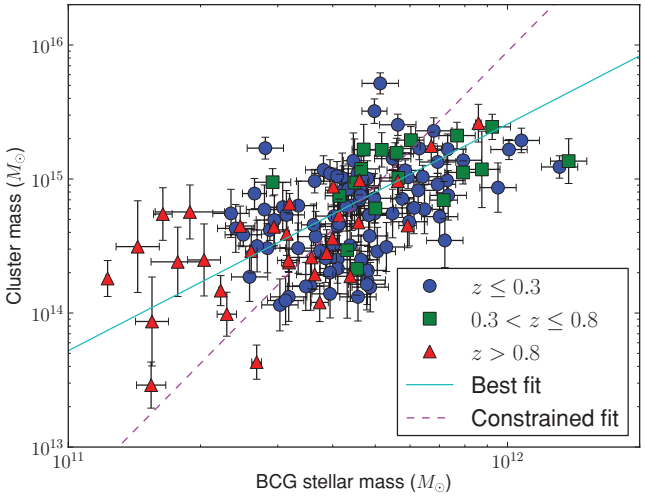

Figure 4. The correlation between the mass of the cluster at the epoch at which it was observed and the stellar mass of the BCG. The different symbols represent different redshift ranges. The solid line is a fit to the data. Setting the index of the power law to the value reported in Hansen et al. (2009) results in a poorer fit to the data (dashed line).

subsamples reflects the volumes probed and the sensitivity limits of the individual surveys that were used to build the subsamples.

We fit a power law to the data using a lognormal distribution to represent the likelihood of getting a certain data point given the model and allowing for additional dispersion by scaling the measurement uncertainties. The index of the power law that corresponds to the maximum of the posterior distribution is 1.6 ± 0.2. Because we treat errors and the amount of extra dispersion in both axes equally, our results are robust to flipping the axes in the fit. The amount of extra dispersion found in the fit corresponds to increasing the size of the error bars by a factor of 1.5.

The index of the power law suggests that clusters accrete mass five times faster than the BCGs accrete stellar mass. Within uncertainties, the index is similar to that found in Stott et al. (2010), who find 2.4 ± 0.6 and Stott et al. (2012) who find 1.3 ± 0.1. Some of the difference between our results and those in Stott et al. (2010, 2012) come from the way the samples are selected and the way the analysis is performed. Our best-fitting index is about a factor of 2 smaller than those reported in earlier works (Lin & Mohr 2004; Popesso et al. 2007; Brough et al. 2008; Hansen et al. 2009). For example, Hansen et al. (2009) find an index of 3.3 between the i-band luminosity (k-corrected to $z = 0.25$) and M_{200}. We redid the fit with the index constrained to this value. The resulting relation is shown in Fig. 4 as the dashed line. It is a poorer fit to the data.

Our fit to the entire sample seems to be largely driven by the clusters in the high-redshift subsample, whereas most of the clusters in Hansen et al. (2009) were at low redshift. This raises the possibility that there is evolution in the index of the power law with redshift. Alternatively, the difference might be caused by redshift-dependent selection effects. In accounting for cluster masses in the following sections, we adopt a conservative approach and examine how our results depend on which index we choose to use. We will find that our conclusions are robust to this choice.

5.3.3 *Accounting for cluster masses*

As foreshadowed earlier, we use two approaches to account for the correlation between cluster mass and BCG stellar mass. We discuss the first approach in this section and discuss the second approach in the section that follows.

In the first approach, we randomly select clusters from the three subsamples until the mass histograms[12] of the subsamples match. Clusters are matched according to the mass they will have by the current epoch. Implicit in this approach is the method we use to estimate how clusters build up their mass with time.

We cannot match all three subsamples simultaneously because trying to get all the histograms to match would result in very few objects per subsample. Instead, we compare the low-redshift subsample with the intermediate- and high-redshift subsamples separately. The method is illustrated in Fig. 5 for the comparison between the low- and high-redshift subsamples.

In order to get a measure of the uncertainties in the derived mass ratios, we do two things. We first perturb the cluster mass by an amount that depends on two sources of error: the uncertainty in the measurement of the mass proxy (X-ray temperature, X-ray gas mass, X-ray luminosity or line-of-sight velocity dispersion) and the intrinsic scatter between the mass proxy and the mass. For masses that are determined from the X-ray gas mass or the X-ray temperature, we assign a scatter of 15 per cent (Mantz et al. 2010). For masses determined from the line-of-sight velocity dispersion, we assign a scatter of 30 per cent (Hicks et al. 2006). For masses inferred from the X-ray luminosity, we use 50 per cent, which we derived earlier. The magnitude of the perturbation is drawn from a lognormal distribution. The s.d. of the distribution is set equal to the two uncertainties added in quadrature.

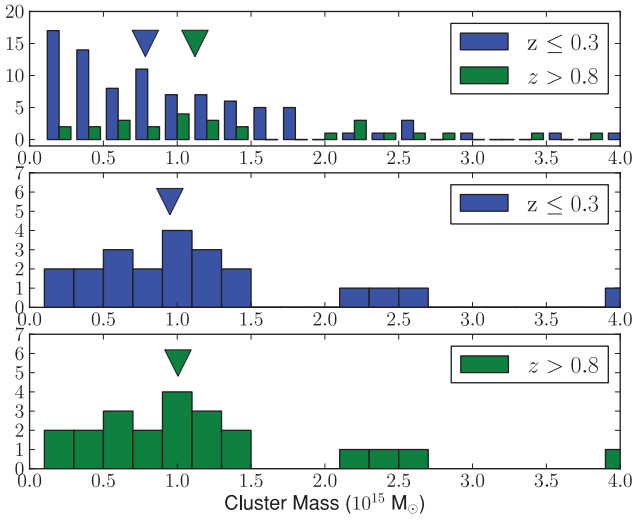

Figure 5. Upper panel: a histogram showing the distributions of cluster mass (extrapolated to the current epoch) for the low- and high-redshift subsamples. The median masses are marked with the downward pointing arrows. Note how the median mass of the two distributions differ and how skewed the low-redshift subsample is with respect to the high-redshift one. Lower two panels: histograms of the re-sampled low- and high-redshift subsamples. They are resampled so that they are identical for a bin width of 2×10^{14} M$_\odot$. The median masses, marked with the downward pointing arrows, are now more similar. There are 23 objects in the lower two histograms.

Secondly, we resample the three subsamples with replacement (bootstrap resampling) to allow for uncertainties that come from sample size. Only then do we try to match the histograms in the three subsamples. We repeat this exercise 100 times for each comparison to create 200 realizations from the data. For each realization, we compute the median BCG stellar mass, the median cluster mass and median redshift. For each comparison, we then average the results from the 100 realizations and get an estimate of the robustness of the results from the variance. The results of the comparisons are listed in Table 8 and shown in Fig. 6. The uncertainty in the last column in Table 8 is computed from the 100 realizations and gives an indication of the robustness of the result. The uncertainties are plotted as the vertical error bars in Fig. 6. No other uncertainties are included in these error bars.

Between $z \sim 0.9$ and $z \sim 0.2$, the stellar mass of BCGs increases by a factor of 1.8 ± 0.3. This is larger than the increase reported in the previous section, which did not account for the correlation between cluster mass and the stellar mass of the BCG.

We repeated our analysis by comparing the stellar mass of BCGs in clusters that have the same mass at the redshift they were observed. This is the method used in Whiley et al. (2008). The results are presented in Table 9. Not surprisingly, due to the correlation between the stellar mass of the BCG and the mass of the cluster, and the considerable growth in cluster mass between $z \sim 1$ and today, the evolution in the stellar mass of the BCG is less evident when clusters are compared in this way.

[12] We use a bin size of 2×10^{14} and the mass the clusters are likely to have by today.

Table 8. BCG mass ratios. The cluster mass distributions are matched using the masses the clusters will have by the current epoch.

Samples a and b	Median redshifts		Median cluster masses		Median BCG masses		BCG mass ratio[a]
	Sample a	Sample b	Sample a	Sample b	Sample a	Sample b	
			(10^{15} M$_\odot$)		(10^{12} M$_\odot$)		
Low (a)–intermediate (b)	0.20	0.40	1.59	1.61	0.54	0.51	0.96 ± 0.20
Low (a)–high (b)	0.17	0.97	0.84	0.84	0.45	0.26	0.58 ± 0.08

[a]Defined as the median stellar mass of subsample b divided by the median stellar mass of subsample a.

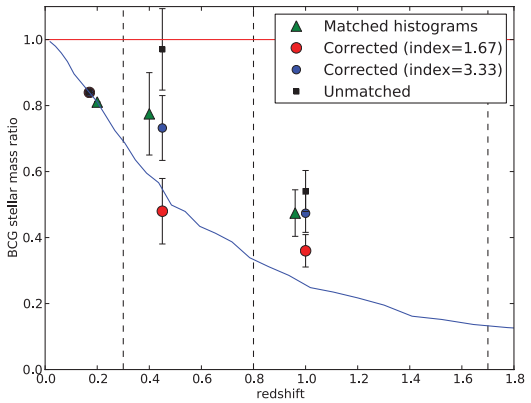

Figure 6. The evolution in the median stellar mass of BCGs as a function of redshift. The green triangles take into account the correlation between cluster mass and the stellar mass of its BCG by matching clusters according to the masses they will have by the present epoch. In a second approach, the red and blue circles account for this correlation using the relations shown in Fig. 4. The small black squares do not account for this correlation. Note how all the points in the high-redshift bin lie below the red line, how the green, blue and red points in the intermediate- and high-redshift bins lie below the black points, and how these points are a better match to the De Lucia & Blaizot (2007) model (solid blue line). All points are normalized so that their low-redshift points land on this model. The vertical dashed lines mark the boundaries of the low-, intermediate- and high-redshift subsamples that are described in the text. The points are plotted at the median redshifts of the subsamples. They differ slightly between the green, red, blue and black points because a more restricted range of clusters is selected when matching cluster masses. See text for details on how the error bars are computed. The red horizontal line represents no mass evolution. The data used in this plot are summarized in Table 10.

Table 10. A summary of the data appearing in Fig. 6.

Method	Redshift	Mass ratio[a]
Matched histograms	0.20	0.81
	0.40	0.77 ± 0.12
	0.96	0.47 ± 0.07
No matching	0.17	0.84
	0.45	0.97 ± 0.12
	1.00	0.54 ± 0.06
Correcting with index 1.67	0.17	0.84
	0.45	0.48 ± 0.10
	1.00	0.36 ± 0.06
Correcting with index 3.33	0.17	0.84
	0.45	0.73 ± 0.10
	1.00	0.47 ± 0.06

[a]The ratios are scaled so that the low-redshift point matches the prediction of De Lucia & Blaizot (2007).

5.3.4 An alternative approach

An alternative approach to account for the correlation between cluster mass and BCG stellar mass is to adjust the BCG stellar mass according to the relation shown as the solid line in Fig. 4. As in the first approach, we use the cluster mass extrapolated to the current epoch and not the mass they had at the epoch they were observed. The results are shown as the red points in Fig. 6. The errors are derived using bootstrap resampling. The data used in Fig. 6 are listed in Table 10.

Compared to the previous approach, we find stronger growth in the BCG stellar mass as a function of redshift and better agreement between the data and the semi-analytic models of De Lucia & Blaizot (2007). However, the result depends on the relation shown in Fig. 4. Adopting the relation found by Hansen et al. (2009) instead of the relation we find, for example, results in less growth (the blue points in Fig. 6). The point at intermediate redshift is affected most, since these clusters will be, by today, three times more massive than clusters in the low-redshift sample (see Table 7), thereby leading to significant adjustments. The point at high redshifts is affected less because these clusters will be, by the current epoch, similar in mass to clusters in the low-redshift sample.

We do not adopt the relation found in Hansen et al. (2009). Instead we use it to demonstrate the sensitivity of the approach to changes in the power-law index. The sample used in Hansen et al. (2009) to compute the relation is restricted to clusters in the redshift range $0.1 \leq z \leq 0.3$. There are also differences in the analysis. Cluster masses in Hansen et al. (2009) are estimated from the optical richness, and BCG masses are estimated from the observer-frame *i*

Table 9. As for Table 8 with the difference that the matching is done using the masses the clusters have at the redshift at which they were observed.

Samples a and b	Median redshifts		Median cluster masses		Median BCG masses		BCG mass ratio[a]
	Sample a	Sample b	Sample a	Sample b	Sample a	Sample b	
			(10^{15} M$_\odot$)		(10^{12} M$_\odot$)		
Low (a)–intermediate (b)	0.20	0.44	1.02	1.06	0.51	0.51	1.02 ± 0.16
Low (a)–high (b)	0.10	1.00	0.33	0.30	0.41	0.29	0.71 ± 0.10

[a]Defined as the median stellar mass of subsample b divided by the median stellar mass of subsample a.

band, which, when combined with the optical selection, may lead to biases that influence the result.

We use the differences in the results between this approach (using the best-fitting power-law index), the approach described in Section 5.3.3, and the approach of not applying any correction as an estimate of the size of the systematic error. Clearly, between the intermediate- and low-redshift samples, the evidence for evolution is marginal. The statistical and systematic uncertainties are too large.

However, between the high- and low-redshift samples, the evidence for evolution is clear and unambiguous. Between $z \sim 0.9$ and $z \sim 0.2$, the stellar mass of BCGs increases by a factor of 1.8 ± 0.3 with a spread of 0.4 spanning the three approaches.

6 DISCUSSION

The semi-analytic model of De Lucia & Blaizot (2007) predicts that BCGs grow by a factor of almost 3 in stellar mass between $z \sim 0.9$ and $z \sim 0.2$. Over the same redshift interval, we observe that BCGs increase their stellar mass by a factor of 1.8 ± 0.3.

Our result depends on the methods we have used to analyse the data and the choice of models that we have used to estimate stellar masses. We discuss each of these in turn, finding that our results are robust.

6.1 Estimating the K_s-band flux

Throughout this paper we have estimated the K_s-band flux using `MAG_AUTO` in SExtractor, which is a Kron-like magnitude (Kron 1980) within an elliptical aperture. Undoubtedly, `MAG_AUTO`, like all other measures of the total magnitude used in the literature, will be systematically biased to low or high values depending on the nature of the object being measured. The bias can occur for a number of reasons, such as the number and brightness nearby neighbours, the presence of intra-cluster light (ICL) and/or a cD envelope, the point spread function (i.e. seeing) and residual errors that come from the imprecise removal of the bright night sky from NIR images. For the purpose of comparing the stellar mass of BCGs at low and high redshifts, the most important aspect of the measurement is that the bias does not change with redshift. In this section we search for evidence of the bias changing with redshift and try to estimate how large this bias may be.

Graham & Driver (2005) noted that Kron-like magnitudes can significantly underestimate the flux of galaxies with Sérsic profiles. We ran our own investigation into the accuracy of `MAG_AUTO` by inserting objects with Sérsic profiles in simulated images. In the simulations, we mimicked the background noise and image quality of the real data. For de Vaucouleur profiles,[13] `MAG_AUTO` misses between 18 and 35 per cent of the flux, depending on the redshift. The trend with redshift is non-monotonic. At $z = 0.1$, 25 per cent of the flux is missed. This decreases to 18 per cent by $z = 0.4$, then increases to 25 per cent by $z = 1.0$ and to 35 per cent by $z = 1.6$. For higher Sérsic indices (we tested indices as high as $n = 8$), higher fractions of the flux are missed by `MAG_AUTO`; however the trend with redshift is the same.

Clearly, if the profiles of BCGs evolve with time, then there will a redshift-dependent bias in the stellar masses that are inferred from the photometry. For example, if low-redshift BCGs had de Vaucouleur profiles and high-redshift BCGs had Sérsic profiles with $n = 8$, then we would *overestimate* the flux of the low-redshift BCGs relative to their distant cousins, and therefore their stellar mass, by around 10 per cent. If the opposite was true (i.e. high-redshift BCGs had de Vaucouleur profiles and low-redshift BCGs had Sérsic profiles with $n = 8$), then we would *underestimate* the flux of the low-redshift BCGs by 3 per cent. The asymmetry is caused by the dependence of how accurately `MAG_AUTO` measures total magnitude with redshift and seeing. Observational constraints on the redshift dependence of the Sérsic index show that the redshift dependence is much weaker than the range of values that we have considered here (Stott et al. 2011).

In our simulations, we neglected errors in the photometry that come from nearby (in projection) galaxies and imprecise sky-subtraction. To investigate these issues, we compare the integrated light profiles of the BCGs measured with version 3.0.4 of GALFIT[14] (Peng 2002). Galaxies neighbouring the BCG were either fitted simultaneously (if they were within 2–3 arcsec of the BCG) or masked as bad pixels (if they were further than this). We used the residual images and the reduced χ^2 of the fit to determine how well the data were described with the model. With the exception of SpARCS-0035 and SpARCS-1638, the BCGs could be modelled satisfactorily (a reduced χ^2 close to one) with a de Vaucouleur profile. The BCGs of both SpARCS-0035 and SpARCS-1638 were better fitted with Sérsic profiles that had a higher Sérsic indices.

For the SpARCS clusters, which have a median redshift of $z \sim 1.1$, the offset between `MAG_AUTO` and the magnitude determined by integrating the fitted GALFIT profile out to infinity have a median value of 0.30 mag (i.e. relative to the integrated GALFIT flux, `MAG_AUTO` underestimates the flux). For clusters in the CNOC1 sample, which have a median redshift of $z \sim 0.28$, the offset between the integrated GALFIT magnitude and `MAG_AUTO` has a median value of 0.49 mag, which is considerably larger than the median value found for the SpARCS clusters.

In part, the difference between the offsets is due to the way the aperture in `MAG_AUTO` is defined. The size of the aperture depends on the seeing convolved profile of the BCG. Since the CNOC1 and SpARCS samples were taken in similar seeing, the apertures for the SpARCS BCGs are affected more by the seeing, since the angular size of the BCGs relative to the seeing disc is smaller. This leads one to using apertures for the SpARCS BCGs that are larger than one would have used if the ratio of the seeing to the angular size of the BCG was the same for both samples. This then leads to a smaller difference for SpARCS BCGs.

The offset between the differences translates directly into a relative offset in the stellar masses of the BCGs in SpARCS and CNOC1. Relative to the stellar masses of the BCGs in the SpARCS clusters, we are underestimating the stellar masses of the BCGs in the CNOC1 clusters by a factor of 1.2. If this offset were applicable to the rest of the BCGs in our low-redshift subsample, then we would be underestimating the growth in BCGs between the low- and high-redshift subsamples by a similar amount. Hence, instead of finding that the mass grows by a factor of 1.8 ± 0.3, we would find that the mass grows by a factor of 2.2.

In this paper, we do not use the integrated magnitude in GALFIT to estimate stellar masses. We make this choice because most of the BCGs in our low-redshift subsample have not been analysed with GALFIT.

[13] The de Vaucouleur profile is equivalent to a Sérsic profile with the Sérsic index, n, set to 4.

[14] http://users.obs.carnegiescience.edu/peng/work/galfit/galfit.html

Instead, we note that there is a source of systematic uncertainty in the relative stellar masses between low and high redshifts that comes from the photometry. By comparing two widely used techniques to do galaxy photometry, we estimate this uncertainty to be ∼20 per cent.

6.2 Stellar masses of the BCGs

In Section 5.2, we described how we used the K_s-band magnitude of BCGs and the predictions of a model that broadly describes the change in the $J - K_s$ colour of BCGs with redshift to estimate their stellar masses. The masses will depend on the model used, so our conclusions are model dependent. To explore how sensitive this dependence is, we re-estimate the masses using another stellar population synthesis code.

Model 5 in Fig. 2 and Table 6 is from M05. The stars in this model formed in a single burst at $z = 4$, have a metallicity that is twice solar and form a red horizontal branch, as found in most metal-rich globular clusters. The model follows the evolution of the $J - K_s$ colour with redshift almost as well as model 3, although it tends to predict redder colours at $z \sim 1.4$.

The M05 and BC03 models differ in several ways. One of the differences most noted in the literature (see Maraston et al. 2006; Marigo et al. 2008, for example) is the treatment of the thermally pulsing asymptotic giant branch (TP-AGB) phase of stellar evolution. This phase significantly affects the optical–NIR colours of SSPs in the age range $0.5 < t < 1.5$ Gyr. Over this age range, the M05 models predict redder optical–NIR colours and, for a given stellar mass, higher NIR luminosities.

As we did for the BC03 models, we normalize the M05 model so that they match the brightness of the BCGs over the redshift interval $0 < z < 0.3$. Using the M05 models, we find that the stellar mass of BCGs at $z = 0.9$ is 1.81 ± 0.26 times less massive than BCGs at $z = 0.2$, which is similar to the results that we derive using the BC03 models.

We do not know if the BC03 models are more appropriate than those in M05; however, we note that recent observations are now suggesting that the contribution from TP-AGB stars to the NIR flux may not be as significant as previously thought (Kriek et al. 2010; Zibetti et al. 2012).

Finally, for a couple of BCGs, we examine how well our stellar mass estimates compare with measurements that are made using more extensive photometric data, a different stellar population model and a different way of estimating total magnitudes. Using 10 broad-band filters extending from 4640 Å to 8.0 μm (rest frame), Rettura et al. (in preparation) estimate a stellar mass of $3.9 \times 10^{11}\,M_\odot$ for the BCG in SpARCS J003550−431224. Our estimate from the K-band photometry is $3.3 \times 10^{11}\,M_\odot$. Rettura et al. (2006), using nine-band photometry, derive a stellar mass of $\sim 2.3 \times 10^{11}\,M_\odot$ for the BCG in RDCS J1252.9−2927. From the K-band photometry, we find $3.3 \times 10^{11}\,M_\odot$.

6.3 Comparison with other results

Our finding of significant evolution in the stellar mass of BCGs with time differs from the findings of a number of authors (Whiley et al. 2008; Collins et al. 2009; Stott et al. 2010). Since the K_s-band magnitudes and $J - K_s$ colours of the BCGs that we have added in this paper are similar to the magnitudes and colours of BCGs from earlier works (Stott et al. 2008, 2010) and since much of our sample consists of BCGs from these works, the reason for the difference lies in the way we have done the analysis.

In part, the difference comes from the way we have compared low- and high-redshift BCGs. In this paper, we first match clusters according to the mass they will have by the current epoch, before comparing the stellar mass of the BCGs they host. Earlier works have done this comparison differently. For example, Whiley et al. (2008) match the clusters according to the mass they had at the redshift they were observed. We repeated our analysis using this approach (see Table 9 and Section 5.3.3) and found that the evidence for evolution became considerably weaker.

The difference may also come from the redshift interval that we use to define the low-redshift subsample. In this paper, we use $z < 0.3$. This is broader than that used by other authors, e.g. Stott et al. (2008). The broader interval allows us to use more objects to determine the stellar mass ratio at the expense of a smaller time interval between the low- and high-redshift samples. We repeated our analysis with the redshift interval for the low-redshift sample set to $z < 0.1$. We find that the stellar mass ratio between the high- and low-redshift subsamples increases slightly to 0.61 ± 0.19. The uncertainty is larger because there are fewer objects in the low-redshift subsample. More significant, however, is that the redshift interval between the low- and high-redshift subsamples increases, thereby increasing the tension between the data and the predictions of the semi-analytic models.

6.4 The build up of stellar mass in BCGs

In semi-analytic models of De Lucia & Blaizot (2007), the stellar masses of BCGs increase by a factor of about 3 between $z \sim 0.9$ and $z \sim 0.2$. Our results suggest that the growth is slower than this. Over the same redshift range, we find the increase to be a factor of 1.8 ± 0.3, suggesting that the model overpredicts the amount of stellar mass by a factor of ∼1.5 – the difference between the blue line and the green triangle in Fig. 6).

In semi-analytic models, most of the build up in stellar mass occurs through dry mergers (both major and minor) with other galaxies. There is ample observational evidence for major mergers in the centres of clusters (Rasmussen et al. 2010; Brough et al. 2011; Bildfell et al. 2012). Brough et al. (2011) in a study of three BCGs at $z \sim 0.1$ with nearby companions found that the companions of two of the BCGs would merge with the BCG within 0.35 Gyr. More dramatic still is the merger that is occurring in the centre of MZ 10451 (Rasmussen et al. 2010).

Evidence for major mergers can also be seen in some of the SpARCS BCGs. For example, the isophotes of the BCG in SpARCS J163435+402151 are distorted, indicating a possible major merger. In this cluster, there is evidence that another major merger is occurring for a galaxy that is almost as bright on the other side of the cluster.

There is also an example in the SpARCS sample of a merger that is likely to happen by today. In the centre of SpARCS J161641+554513, there is a galaxy that is within 20 kpc projected distance of the BCG. The velocity difference between the two galaxies is $\sim 140\,\mathrm{km\,s^{-1}}$, and the companion is almost as bright as the BCG (see Fig. 1). It is highly likely that these two galaxies would have merged by now. Additional examples of likely major mergers can be found in RX J0848.9+4452 (Yamada et al. 2002) and RDCS J1252−2927 (Collins et al. 2009).

While it is clear that mergers do occur, it is not yet clear what fraction of the stars in the merging galaxies end up in the BCG and what fraction end up distributed throughout the cluster, appearing as ICL. The apparent lack of evolution in the stellar mass of BCGs that was found in earlier work suggested that the contribution to

the ICL was close to 100 per cent (Whiley et al. 2008; Collins et al. 2009; Stott et al. 2010). Our results suggest that it is closer to 50 per cent. High-resolution simulations suggest that 50–80 per cent of the mass of mergers will be distributed throughout the cluster (Conroy, Wechsler & Kravtsov 2007; Puchwein et al. 2010). Recent measurements of the ICL show that it grows relative to the total cluster light by a factor of 2–4 since $z \sim 1$ (Burke et al. 2012).

It is possible that some of the BCGs in our sample are increasing their stellar mass through star formation. Out of the 12 SpARCS BCGs, five show emission from the [O II] $\lambda\lambda$ 3726,3728 doublet, which is an indicator of star formation and/or active galactic nuclei (AGN) activity. It is unlikely that most of the [O II] emission that we detect comes from star formation. Over 70 per cent of low-redshift BCGs that have detectable [O II] emission have line ratios that are consistent with the line ratios of AGN (von der Linden et al. 2007). Our spectra do not cover the lines that can be used to separate AGN activity and star formation, such as the [O III] $\lambda\lambda$ 4959,5007 doublet, Hβ, Hα and [N II]λ 6584.

If we were to assume that the [O II] emission did come from star formation entirely and if we ignore dust, then the average [O II] line flux corresponds to a star formation rate of about 1 solar mass per year, using equation (4) in Kewley, Geller & Jansen (2004) to make the conversion between [O II] line flux and the star formation rate. At these rates, star formation will not contribute much to the overall stellar mass of the BCG, even if they were to continue forming stars at this rate until today.

7 SUMMARY AND CONCLUSIONS

Using NIR photometry from the literature (Stott et al. 2008, 2010) and photometry from an analysis of imaging data that we obtained using several ground-based near-IR cameras, we have investigated how the stellar masses of BCGs change with redshift. The BCGs in our sample cover a broad redshift range, from $z = 0.03$ to $z = 1.63$, which covers 9.8 Gyr, or 70 per cent of the history of the universe.

To estimate the stellar mass of the BCGs, we compare the K_s-band flux with the predictions from a stellar population synthesis model that matches the $J - K_s$ colour of the BCGs over the entire redshift range covered by the data.

We then compare mass of BCGs at low and high redshifts. After accounting for the correlation between BCG stellar mass and cluster mass, we find that, between $z = 0.9$ and $z = 0.2$, BCGs, on average, grow in mass by a factor of 1.8 ± 0.3. Our result is not weakened if we choose other methods to estimate the K_s-band flux or if we choose other stellar population synthesis models to infer the mass. The systematic uncertainty coming from the photometry is probably the dominant source of systematic uncertainty in our analysis and affects our estimates of the growth rate by around 20 per cent.

Our conclusions differ from those of earlier works (Collins et al. 2009; Stott et al. 2010). In part, this is due to the way we have accounted for the correlation between the mass of the BCG and the mass of the cluster and to the redshift intervals that we use to define the low- and high-redshift subsamples.

Our measurements are now in better agreement with the predictions of semi-analytic models for the growth of stellar mass in BCGs (De Lucia & Blaizot 2007). However, there is still some tension between the data and these models, which predict growth rates that are a factor of 1.5 higher.

We find direct evidence that some of the BCGs in our sample are building up their stellar mass through star formation and major mergers. However, star formation, while present in some of BCGs, is at low levels. At these levels, star formation cannot be the dominant mechanism for the build up of stellar mass in BCGs over the last 10 billion years. The build-up mainly occurs through mergers, of which some are clearly major.

ACKNOWLEDGMENTS

The authors thank John Stott, Chris Collins and Gabriela DeLucia for providing us with the tabulated data from their papers and for useful discussions. The data in this paper were based in part on observations obtained with WIRCam, a joint project of CFHT, Taiwan, Korea, Canada, France, at the CFHT which is operated by the National Research Council (NRC) of Canada, the Institute National des Sciences de l'Univers of the Centre National de la Recherche Scientifique of France, and the University of Hawaii. Based in part on observations taken at the ESO Paranal Observatory (ESO programmes 084.A-0214, 085.A-0166 and 085.A-0613). Based in part on observations taken at the CTIO. RD gratefully acknowledges the support provided by the BASAL Center for Astrophysics and Associated Technologies (CATA), and by FONDECYT grant N. 1100540. CL is the recipient of an Australian Research Council Future Fellowship (program number FT0992259). GW gratefully acknowledges support from NSF grant AST-0909198.

REFERENCES

Aragon-Salamanca A., Baugh C. M., Kauffmann G., 1998, MNRAS, 297, 427
Baugh C. M., 2006, Rep. Progress Phys., 69, 3101
Bertin E., Arnouts S., 1996, A&AS, 117, 393
Bildfell C., Hoekstra H., Babul A., Mahdavi A., 2008, MNRAS, 389, 1637
Bildfell C. et al., 2012, MNRAS, 425, 204
Boylan-Kolchin M., Springel V., White S. D. M., Jenkins A., Lemson G., 2009, MNRAS, 398, 1150
Brough S., Couch W. J., Collins C. A., Jarrett T., Burke D. J., Mann R. G., 2008, MNRAS, 385, L103
Brough S., Tran K.-V., Sharp R. G., von der Linden A., Couch W. J., 2011, MNRAS, 414, L80
Bruzual G., Charlot S., 2003, MNRAS, 344, 1000 (BC03)
Bullock J. S., Kolatt T. S., Sigad Y., Somerville R. S., Kravtsov A. V., Klypin A. A., Primack J. R., Dekel A., 2001, MNRAS, 321, 559
Burke D. J., Collins C. A., Mann R. G., 2000, ApJ, 532, L105
Burke C., Collins C. A., Stott J. P., Hilton M., 2012, MNRAS, 425, 2058
Casali M. et al., 2006, in McLean I. S., Iye M., eds, Proc. SPIE Vol. 6269, Ground-based and Airborne Instrumentation for Astronomy. SPIE, Bellingham, p. 29
Chabrier G., 2003, PASP, 115, 763
Collins C. A. et al., 2009, Nat, 458, 603
Conroy C., Wechsler R. H., Kravtsov A. V., 2007, ApJ, 668, 826
De Lucia G., Blaizot J., 2007, MNRAS, 375, 2
de Propris R., Eisenhardt P. R., Stanford S. A., Dickinson M., 1998, ApJ, 503, L45
Demarco R. et al., 2010, ApJ, 711, 1185
Ebeling H., Voges W., Bohringer H., Edge A. C., Huchra J. P., Briel U. G., 1996, MNRAS, 281, 799
Ebeling H., Edge A. C., Bohringer H., Allen S. W., Crawford C. S., Fabian A. C., Voges W., Huchra J. P., 1998, MNRAS, 301, 881
Ebeling H., Edge A. C., Allen S. W., Crawford C. S., Fabian A. C., Huchra J. P., 2000, MNRAS, 318, 333
Ebeling H., Barrett E., Donovan D., Ma C.-J., Edge A. C., van Speybroeck L., 2007, ApJ, 661, L33
Ebeling H., Edge A. C., Mantz A., Barrett E., Henry J. P., Ma C. J., van Speybroeck L., 2010, MNRAS, 407, 83
Edge A. C., 1991, MNRAS, 250, 103
Fakhouri O., Ma C.-P., Boylan-Kolchin M., 2010, MNRAS, 406, 2267

Gioia I. M., Maccacaro T., Schild R. E., Wolter A., Stocke J. T., Morris S. L., Henry J. P., 1990, ApJS, 72, 567
Graham A. W., Driver S. P., 2005, Publ. Astron. Soc. Aust., 22, 118
Hansen S. M., Sheldon E. S., Wechsler R. H., Koester B. P., 2009, ApJ, 699, 1333
Hicks A. K., Ellingson E., Hoekstra H., Yee H. K. C., 2006, ApJ, 652, 232
Hu W., Kravtsov A. V., 2003, ApJ, 584, 702
Kewley L. J., Geller M. J., Jansen R. A., 2004, AJ, 127, 2002
Kriek M. et al., 2010, ApJ, 722, L64
Kron R. G., 1980, ApJS, 43, 305
Lidman C. et al., 2008, A&A, 489, 981
Lin Y.-T., Mohr J. J., 2004, ApJ, 617, 879
Loubser S. I., Sánchez-Blázquez P., Sansom A. E., Soechting I. K., 2009, MNRAS, 398, 133
Mantz A., Allen S. W., Ebeling H., Rapetti D., Drlica-Wagner A., 2010, MNRAS, 406, 1773
Maraston C., 2005, MNRAS, 362, 799 (M05)
Maraston C., Daddi E., Renzini A., Cimatti A., Dickinson M., Papovich C., Pasquali A., Pirzkal N., 2006, ApJ, 652, 85
Marigo P., Girardi L., Bressan A., Groenewegen M. A. T., Silva L., Granato G. L., 2008, A&A, 482, 883
Meyers J. et al., 2012, ApJ, 750, 1
Muzzin A., Yee H. K. C., Hall P. B., Ellingson E., Lin H., 2007a, ApJ, 659, 1106
Muzzin A., Yee H. K. C., Hall P. B., Lin H., 2007b, ApJ, 663, 150
Muzzin A., Wilson G., Lacy M., Yee H. K. C., Stanford S. A., 2008, ApJ, 686, 966
Muzzin A. et al., 2009, ApJ, 698, 1934
Muzzin A. et al., 2012, ApJ, 746, 188
Navarro J. F., Frenk C. S., White S. D. M., 1997, ApJ, 490, 493
Nelson A. E., Gonzalez A. H., Zaritsky D., Dalcanton J. J., 2002, ApJ, 566, 103
Peng C. Y., 2002, AJ, 124, 294
Pirard J.-F. et al., 2004, in Moorwood A. F. M., Iye M., eds, Proc. SPIE Vol. 5492, Ground-based Instrumentation for Astronomy. SPIE, Bellingham, p. 1763
Popesso P., Biviano A., Böhringer H., Romaniello M., 2007, A&A, 464, 451
Puchwein E., Springel V., Sijacki D., Dolag K., 2010, MNRAS, 406, 936
Puget P. et al., 2004, in Moorwood A. F. M., Iye M., eds, Proc. SPIE Vol. 5492, Ground-based Instrumentation for Astronomy. SPIE, Bellingham, p. 978
Rasmussen J., Mulchaey J. S., Bai L., Ponman T. J., Raychaudhury S., Dariush A., 2010, ApJ, 717, 958
Rettura A. et al., 2006, A&A, 458, 717
Salpeter E. E., 1955, ApJ, 121, 161
Sehgal N. et al., 2012, preprint (arXiv:1205.2369)
Skrutskie M. F. et al., 2006, AJ, 131, 1163,
Springel V. et al., 2005, Nat, 435, 629
Stott J. P., Edge A. C., Smith G. P., Swinbank A. M., Ebeling H., 2008, MNRAS, 384, 1502
Stott J. P. et al., 2010, ApJ, 718, 23
Stott J. P., Collins C. A., Burke C., Hamilton-Morris V., Smith G. P., 2011, MNRAS, 414, 445
Stott J. P. et al., 2012, MNRAS, 422, 2213
van der Bliek N. S. et al., 2004, in Moorwood A. F. M., Iye M., eds, Proc. SPIE Vol. 5492, Ground-based Instrumentation for Astronomy. SPIE, Bellingham, p. 1582
von der Linden A., Best P. N., Kauffmann G., White S. D. M., 2007, MNRAS, 379, 867
Wechsler R. H., Bullock J. S., Primack J. R., Kravtsov A. V., Dekel A., 2002, ApJ, 568, 52
Whiley I. M. et al., 2008, MNRAS, 387, 1253
Wilson G. et al., 2009, ApJ, 698, 1943
Yamada T., Koyama Y., Nakata F., Kajisawa M., Tanaka I., Kodama T., Okamura S., De Propris R., 2002, ApJ, 577, L89
Yee H. K. C., Ellingson E., Carlberg R. G., 1996, ApJS, 102, 269
Zibetti S., Gallazzi A., Charlot S., Pasquali A., Pierini D., 2012, preprint (arXiv:1203.4571)

APPENDIX A: DATA

In Tables A1, A2 and A3, we list the names of the clusters, their redshifts, their masses and the mass proxy used to determine masses. Two estimates of the mass are provided. The first is computed from the mass proxy and represents the mass of the cluster when it was observed. The errors in the cluster masses only include the error in the mass proxy. They do not include the intrinsic scatter in the relation between mass and mass proxy. The second mass extrapolates the first mass to the current epoch by integrating the mean mass accretion rates in Fakhouri et al. (2010). The error does not take into account the intrinsic scatter in the accretion rates. Wechsler et al. (2002) estimate that between $z = 1$ and $z = 0$, the final mass of a $10^{14}\,M_{\odot}$ halo can scatter by 20–30 per cent. Also listed in the table are the magnitudes and colours of the BCGs. If available, we also list the errors in these quantities. Excluding the BCGs in the SpARCS and CNOC1 clusters, the magnitudes and colours of the BCGs in these tables were obtained from Stott et al. (2008, 2010) and J. P. Stott (private communication). The model-dependent masses, which have been adjusted to account for the loss of mass due to supernova explosions and stellar winds, are listed in the final column. Not all clusters have mass measurements in the papers listed in the main body of the paper. These clusters are listed in Table A4.

Table A1. The low-redshift subsample.

		Cluster			BCG		
Name	Redshift	Mass ($10^{15}\,M_\odot$)	Mass today ($10^{15}\,M_\odot$)	Mass proxy	K_s (mag)	$J-K_s$ (mag)	Stellar mass ($10^{12}\,M_\odot$)
Abell 1902	0.160	$0.48^{+0.06}_{-0.06}$	$0.61^{+0.08}_{-0.08}$	X-ray luminosity	12.63	1.37	0.59
Abell 193	0.049	$0.18^{+0.03}_{-0.03}$	$0.20^{+0.03}_{-0.03}$	X-ray luminosity	10.43	1.06	0.48
Abell 1930	0.131	$0.38^{+0.05}_{-0.05}$	$0.48^{+0.07}_{-0.07}$	X-ray luminosity	12.47	1.10	0.48
Abell 1991	0.059	$0.16^{+0.02}_{-0.02}$	$0.18^{+0.02}_{-0.02}$	X-ray luminosity	11.15	1.01	0.35
Abell 2029	0.077	$1.2^{+0.2}_{-0.2}$	$1.4^{+0.2}_{-0.2}$	X-ray gas mass	10.30	1.13	1.31
Abell 2034	0.113	$0.89^{+0.13}_{-0.13}$	$1.2^{+0.2}_{-0.2}$	X-ray gas mass	12.21	1.07	0.46
Abell 2052	0.035	$0.25^{+0.02}_{-0.02}$	$0.28^{+0.02}_{-0.02}$	X-ray luminosity	9.88	1.00	0.41
Abell 2065	0.073	$0.43^{+0.04}_{-0.04}$	$0.48^{+0.05}_{-0.05}$	X-ray luminosity	12.03	1.15	0.24
Abell 2072	0.127	$0.31^{+0.06}_{-0.06}$	$0.39^{+0.08}_{-0.08}$	X-ray luminosity	12.82	1.23	0.33
Abell 2107	0.041	$0.13^{+0.02}_{-0.02}$	$0.15^{+0.02}_{-0.02}$	X-ray luminosity	10.10	1.00	0.45
Abell 2124	0.066	$0.16^{+0.03}_{-0.03}$	$0.17^{+0.03}_{-0.03}$	X-ray luminosity	11.05	1.05	0.48
Abell 2175	0.095	$0.29^{+0.03}_{-0.03}$	$0.32^{+0.04}_{-0.04}$	X-ray luminosity	11.78	1.18	0.50
Abell 2204	0.152	$1.4^{+0.2}_{-0.2}$	$1.8^{+0.3}_{-0.3}$	X-ray gas mass	12.23	1.14	0.78
Abell 2244	0.097	$0.82^{+0.15}_{-0.15}$	$0.94^{+0.17}_{-0.17}$	X-ray gas mass	11.59	1.11	0.62
Abell 2259	0.164	$0.55^{+0.08}_{-0.08}$	$0.71^{+0.10}_{-0.10}$	X-ray luminosity	12.77	1.19	0.54
Abell 2345	0.177	$0.76^{+0.13}_{-0.13}$	$0.98^{+0.17}_{-0.17}$	X-ray luminosity	12.60	1.24	0.72
Abell 2377	0.081	$0.31^{+0.05}_{-0.05}$	$0.34^{+0.06}_{-0.06}$	X-ray luminosity	12.07	1.09	0.28
Abell 2382	0.062	$0.12^{+0.03}_{-0.03}$	$0.13^{+0.03}_{-0.03}$	X-ray luminosity	11.43	1.06	0.30
Abell 2384	0.094	$0.55^{+0.06}_{-0.06}$	$0.63^{+0.07}_{-0.07}$	X-ray luminosity	12.59	1.15	0.23
Abell 2402	0.081	$0.22^{+0.04}_{-0.04}$	$0.24^{+0.05}_{-0.05}$	X-ray luminosity	11.67	1.17	0.41
Abell 2415	0.058	$0.19^{+0.03}_{-0.03}$	$0.21^{+0.03}_{-0.03}$	X-ray luminosity	11.46	1.05	0.26
Abell 2426	0.098	$0.44^{+0.07}_{-0.07}$	$0.50^{+0.08}_{-0.08}$	X-ray luminosity	12.07	1.02	0.41
Abell 2428	0.085	$0.25^{+0.05}_{-0.05}$	$0.28^{+0.05}_{-0.05}$	X-ray luminosity	11.64	1.07	0.46
Abell 2443	0.108	$0.31^{+0.05}_{-0.05}$	$0.39^{+0.06}_{-0.06}$	X-ray luminosity	11.98	1.13	0.53
Abell 2457	0.059	$0.16^{+0.04}_{-0.04}$	$0.18^{+0.04}_{-0.04}$	X-ray luminosity	10.83	1.03	0.48
Abell 2495	0.078	$0.29^{+0.04}_{-0.04}$	$0.33^{+0.04}_{-0.04}$	X-ray luminosity	11.69	1.09	0.37
Abell 2496	0.123	$0.35^{+0.11}_{-0.11}$	$0.44^{+0.14}_{-0.14}$	X-ray luminosity	11.92	1.17	0.71
Abell 2589	0.042	$0.20^{+0.02}_{-0.02}$	$0.22^{+0.02}_{-0.02}$	X-ray luminosity	10.31	1.04	0.39
Abell 2593	0.043	$0.14^{+0.02}_{-0.02}$	$0.16^{+0.02}_{-0.02}$	X-ray luminosity	10.36	1.02	0.39
Abell 2597	0.085	$0.38^{+0.07}_{-0.07}$	$0.43^{+0.08}_{-0.08}$	X-ray gas mass	12.31	1.01	0.25
Abell 2622	0.062	$0.13^{+0.02}_{-0.02}$	$0.15^{+0.02}_{-0.02}$	X-ray luminosity	11.38	1.01	0.32
Abell 2626	0.057	$0.21^{+0.02}_{-0.02}$	$0.23^{+0.02}_{-0.02}$	X-ray luminosity	10.75	1.09	0.48
Abell 2627	0.126	$0.32^{+0.06}_{-0.06}$	$0.41^{+0.08}_{-0.08}$	X-ray luminosity	12.51	1.22	0.43
Abell 2717	0.050	$0.12^{+0.02}_{-0.02}$	$0.14^{+0.02}_{-0.02}$	X-ray luminosity	10.94	1.06	0.31
Abell 2734	0.062	$0.26^{+0.03}_{-0.03}$	$0.29^{+0.03}_{-0.03}$	X-ray luminosity	11.17	1.05	0.38
Abell 376	0.049	$0.16^{+0.02}_{-0.02}$	$0.18^{+0.02}_{-0.02}$	X-ray luminosity	10.78	1.11	0.35
Abell 399	0.072	$0.52^{+0.05}_{-0.05}$	$0.59^{+0.06}_{-0.06}$	X-ray luminosity	10.84	1.01	0.70
Abell 401	0.074	$1.3^{+0.2}_{-0.2}$	$1.5^{+0.2}_{-0.2}$	X-ray gas mass	10.91	1.22	0.69
Abell 115	0.197	$1.0^{+0.2}_{-0.2}$	$1.3^{+0.2}_{-0.2}$	X-ray luminosity	13.40	1.25	0.41
Abell 1201	0.169	$0.53^{+0.09}_{-0.09}$	$0.68^{+0.12}_{-0.12}$	X-ray luminosity	13.16	1.29	0.40
Abell 1204	0.171	$0.59^{+0.09}_{-0.09}$	$0.76^{+0.12}_{-0.12}$	X-ray luminosity	13.58	1.12	0.28
Abell 1246	0.190	$0.62^{+0.10}_{-0.10}$	$0.79^{+0.13}_{-0.13}$	X-ray luminosity	13.67	1.32	0.30
Abell 1423	0.213	$1.2^{+0.3}_{-0.3}$	$1.8^{+0.4}_{-0.4}$	X-ray gas mass	13.65	1.41	0.38
Abell 1553	0.165	$0.59^{+0.09}_{-0.09}$	$0.76^{+0.11}_{-0.11}$	X-ray luminosity	12.60	1.11	0.64
Abell 1682	0.234	$1.7^{+0.4}_{-0.4}$	$2.5^{+0.7}_{-0.7}$	X-ray gas mass	13.12	1.31	0.72
Abell 1704	0.221	$0.63^{+0.11}_{-0.11}$	$0.92^{+0.17}_{-0.17}$	X-ray luminosity	13.56	1.23	0.43
Abell 1758	0.279	$0.87^{+0.14}_{-0.14}$	$1.3^{+0.2}_{-0.2}$	X-ray luminosity	13.96	1.38	0.45
Abell 1763	0.223	$2.3^{+0.5}_{-0.5}$	$3.5^{+0.7}_{-0.7}$	X-ray gas mass	13.11	1.33	0.67
Abell 1835	0.253	$1.7^{+0.2}_{-0.2}$	$2.5^{+0.3}_{-0.3}$	X-ray gas mass	12.92	1.44	0.99

© 2012 The Authors, MNRAS **427,** 550–568
Monthly Notices of the Royal Astronomical Society © 2012 RAS

Table A1 – *continued*

Name	Redshift	Cluster Mass (10^{15} M$_\odot$)	Mass today (10^{15} M$_\odot$)	Mass proxy	BCG K_s (mag)	BCG $J-K_s$ (mag)	BCG Stellar mass (10^{12} M$_\odot$)
Abell 1914	0.171	$1.4^{+0.2}_{-0.2}$	$1.9^{+0.3}_{-0.3}$	X-ray gas mass	12.85	1.24	0.54
Abell 1961	0.232	$0.55^{+0.10}_{-0.10}$	$0.81^{+0.14}_{-0.14}$	X-ray luminosity	13.52	1.34	0.49
Abell 2009	0.153	$0.70^{+0.10}_{-0.10}$	$0.91^{+0.13}_{-0.13}$	X-ray luminosity	12.83	1.19	0.46
Abell 209	0.209	$1.7^{+0.3}_{-0.3}$	$2.6^{+0.4}_{-0.4}$	X-ray gas mass	13.07	1.39	0.62
Abell 2111	0.229	$1.1^{+0.2}_{-0.2}$	$1.7^{+0.4}_{-0.4}$	X-ray gas mass	13.75	1.35	0.39
Abell 2163	0.203	$5.2^{+0.7}_{-0.7}$	$8.2^{+1.1}_{-1.1}$	X-ray gas mass	13.24	1.74	0.51
Abell 2218	0.176	$0.96^{+0.16}_{-0.16}$	$1.3^{+0.2}_{-0.2}$	X-ray gas mass	13.35	1.11	0.36
Abell 2219	0.226	$2.5^{+0.3}_{-0.3}$	$3.9^{+0.5}_{-0.5}$	X-ray gas mass	13.34	1.36	0.55
Abell 2254	0.178	$0.62^{+0.09}_{-0.09}$	$0.80^{+0.12}_{-0.12}$	X-ray luminosity	13.19	1.27	0.42
Abell 2261	0.224	$1.9^{+0.4}_{-0.4}$	$3.0^{+0.6}_{-0.6}$	X-ray gas mass	12.62	1.42	1.06
Abell 2445	0.165	$0.37^{+0.08}_{-0.08}$	$0.47^{+0.10}_{-0.10}$	X-ray luminosity	13.22	1.18	0.36
Abell 2561	0.163	$0.32^{+0.08}_{-0.08}$	$0.40^{+0.10}_{-0.10}$	X-ray luminosity	13.53	1.18	0.27
Abell 521	0.248	$1.5^{+0.2}_{-0.2}$	$2.3^{+0.4}_{-0.4}$	X-ray gas mass	13.53	1.33	0.55
Abell 586	0.171	$0.82^{+0.12}_{-0.12}$	$1.1^{+0.2}_{-0.2}$	X-ray luminosity	13.13	1.23	0.42
Abell 661	0.288	$0.98^{+0.21}_{-0.21}$	$1.5^{+0.3}_{-0.3}$	X-ray luminosity	13.53	1.31	0.71
Abell 665	0.182	$1.7^{+0.2}_{-0.2}$	$2.2^{+0.3}_{-0.3}$	X-ray gas mass	13.69	1.23	0.28
Abell 68	0.255	$1.0^{+0.2}_{-0.2}$	$1.5^{+0.3}_{-0.2}$	X-ray gas mass	13.51	1.43	0.58
Abell 750	0.180	$0.72^{+0.12}_{-0.12}$	$0.93^{+0.15}_{-0.15}$	X-ray luminosity	13.05	1.31	0.49
Abell 773	0.217	$1.2^{+0.1}_{-0.1}$	$1.7^{+0.2}_{-0.2}$	X-ray gas mass	13.22	1.42	0.58
Abell 907	0.153	$0.63^{+0.09}_{-0.09}$	$0.81^{+0.12}_{-0.12}$	X-ray luminosity	13.18	1.32	0.33
Abell 963	0.206	$0.91^{+0.13}_{-0.13}$	$1.4^{+0.2}_{-0.2}$	X-ray gas mass	12.94	1.37	0.68
RX J1720.1+2638	0.164	$1.1^{+0.1}_{-0.1}$	$1.4^{+0.1}_{-0.1}$	X-ray luminosity	12.97	1.21	0.45
RX J2129.6+0005	0.235	$1.0^{+0.2}_{-0.2}$	$1.5^{+0.3}_{-0.2}$	X-ray gas mass	13.27	1.37	0.63
Zw1432	0.186	$0.46^{+0.11}_{-0.11}$	$0.59^{+0.14}_{-0.14}$	X-ray luminosity	13.31	1.31	0.41
Zw1693	0.225	$0.61^{+0.15}_{-0.15}$	$0.89^{+0.23}_{-0.23}$	X-ray luminosity	13.24	1.38	0.60
Zw1883	0.194	$0.54^{+0.13}_{-0.13}$	$0.69^{+0.17}_{-0.17}$	X-ray luminosity	13.22	1.28	0.48
Zw2089	0.230	$0.42^{+0.05}_{-0.05}$	$0.60^{+0.08}_{-0.08}$	X-ray gas mass	14.10	1.40	0.28
Zw2379	0.205	$0.49^{+0.10}_{-0.10}$	$0.71^{+0.15}_{-0.15}$	X-ray luminosity	13.86	1.27	0.29
Zw2701	0.214	$0.54^{+0.09}_{-0.09}$	$0.78^{+0.14}_{-0.14}$	X-ray gas mass	13.40	1.30	0.48
Zw348	0.255	$0.76^{+0.16}_{-0.16}$	$1.1^{+0.2}_{-0.2}$	X-ray luminosity	13.78	1.43	0.45
Zw3916	0.206	$0.54^{+0.08}_{-0.08}$	$0.78^{+0.12}_{-0.12}$	X-ray luminosity	13.80	1.31	0.31
Zw5247	0.195	$1.1^{+0.3}_{-0.3}$	$1.4^{+0.3}_{-0.3}$	X-ray gas mass	13.41	1.28	0.40
Zw5768	0.266	$0.86^{+0.14}_{-0.14}$	$1.3^{+0.2}_{-0.2}$	X-ray luminosity	13.08	1.25	0.93
Zw7215	0.292	$0.84^{+0.17}_{-0.17}$	$1.2^{+0.3}_{-0.3}$	X-ray luminosity	14.12	1.45	0.43
Abell 2390	0.228	$3.2^{+0.6}_{-0.5}$	$5.0^{+0.9}_{-0.8}$	X-ray temperature	13.49 ± 0.07	...	0.49
MS0440+02	0.197	$1.4^{+0.8}_{-0.3}$	$1.8^{+1.1}_{-0.4}$	X-ray temperature	13.34 ± 0.05	...	0.44
MS0451+02	0.201	$0.78^{+0.20}_{-0.15}$	$1.2^{+0.3}_{-0.2}$	X-ray temperature	13.94 ± 0.07	...	0.26
MS0839+29	0.193	$0.32^{+0.05}_{-0.05}$	$0.41^{+0.07}_{-0.06}$	X-ray temperature	13.41 ± 0.06	...	0.40
MS1006+12	0.261	$1.0^{+0.3}_{-0.3}$	$1.5^{+0.5}_{-0.4}$	X-ray temperature	13.79 ± 0.07	...	0.47
MS1231+15	0.235	$0.46^{+0.14}_{-0.14}$	$0.66^{+0.21}_{-0.21}$	Velocity dispersion	13.89 ± 0.07	...	0.36
MS1455+22	0.257	$0.71^{+0.25}_{-0.16}$	$1.0^{+0.4}_{-0.2}$	X-ray temperature	13.56 ± 0.06	...	0.57

Table A2. The intermediate-redshift subsample.

		Cluster				BCG	
Name	Redshift	Mass ($10^{15}\,M_\odot$)	Mass today ($10^{15}\,M_\odot$)	Mass proxy	K_s (mag)	$J-K_s$ (mag)	Stellar mass ($10^{12}\,M_\odot$)
MACS J0018.5+1626	0.541	$1.7^{+0.5}_{0.5}$	$3.9^{+1.3}_{1.3}$	X-ray temperature	15.35	1.52	0.50
MACS J0025.4−1222	0.478	$0.95^{+0.21}_{0.21}$	$1.9^{+0.4}_{0.4}$	X-ray temperature	15.70	1.67	0.28
MACS J0257.6−2209	0.504	$2.1^{+0.4}_{0.4}$	$5.0^{+1.2}_{1.2}$	X-ray temperature	14.77	1.61	0.74
MACS J0404.6+1109	0.358	$1.2^{+1.1}_{1.1}$	$2.0^{+2.0}_{2.0}$	X-ray temperature	13.82	...	0.85
MACS J0429.6−0253	0.397	$1.4^{+0.6}_{0.6}$	$2.4^{+1.1}_{1.1}$	X-ray temperature	13.58	...	1.34
MACS J0454.1−0300	0.550	$1.0^{+0.3}_{0.3}$	$2.3^{+0.8}_{0.8}$	X-ray temperature	15.29	1.58	0.54
MACS J0647.7+7015	0.584	$2.5^{+0.5}_{0.5}$	$6.0^{+1.2}_{1.2}$	X-ray temperature	14.87	1.76	0.89
MACS J0744.8+3927	0.686	$1.1^{+0.2}_{0.2}$	$3.0^{+0.5}_{0.5}$	X-ray temperature	15.33	1.88	0.76
MACS J2129.4−0741	0.570	$1.2^{+0.2}_{0.2}$	$2.7^{+0.6}_{0.6}$	X-ray temperature	15.57	1.72	0.45
MACS J2245.0+2637	0.301	$0.60^{+0.14}_{0.14}$	$1.00^{+0.25}_{0.25}$	X-ray temperature	14.03	...	0.49
MS0016+16	0.547	$1.6^{+0.4}_{-0.3}$	$3.7^{+1.0}_{-0.8}$	X-ray temperature	15.29 ± 0.08	...	0.54
MS0302+16	0.425	$0.29^{+0.65}_{-0.13}$	$0.53^{+1.30}_{-0.25}$	X-ray temperature	15.01 ± 0.07	...	0.42
MS0451−03	0.539	$2.0^{+0.4}_{-0.4}$	$4.6^{+1.1}_{-1.0}$	X-ray temperature	15.18 ± 0.07	...	0.58
MS1008−12	0.306	$0.70^{+0.24}_{-0.16}$	$1.2^{+0.4}_{-0.3}$	X-ray temperature	13.68 ± 0.08	...	0.70
MS1224+20	0.326	$0.75^{+0.25}_{-0.25}$	$1.3^{+0.4}_{-0.4}$	Velocity dispersion	14.41 ± 0.08	...	0.41
MS1358+62	0.329	$1.7^{+0.9}_{-0.4}$	$2.9^{+1.6}_{-0.7}$	X-ray temperature	14.29 ± 0.06	...	0.46
MS1512+36	0.373	$0.21^{+0.12}_{-0.08}$	$0.34^{+0.20}_{-0.13}$	X-ray temperature	14.63 ± 0.08	...	0.44
MS1621+26	0.427	$0.94^{+1.04}_{-0.47}$	$1.8^{+2.2}_{-1.0}$	X-ray temperature	14.98 ± 0.07	...	0.44

Table A3. The high-redshift subsample.

		Cluster				BCG	
Name	Redshift	Mass ($10^{15}\,M_\odot$)	Mass today ($10^{15}\,M_\odot$)	Mass proxy	K_s (mag)	$J-K_s$ (mag)	Stellar mass ($10^{12}\,M_\odot$)
SpARCS J003442−430752	0.867	$0.36^{+0.16}_{-0.19}$	$1.1^{+0.6}_{-0.6}$	Velocity dispersion	16.52 ± 0.04	1.86 ± 0.03	0.38
SpARCS J003645−441050	0.867	$0.45^{+0.16}_{-0.14}$	$1.4^{+0.6}_{-0.5}$	Velocity dispersion	16.09 ± 0.05	1.84 ± 0.03	0.56
SpARCS J161314+564930	0.873	$2.6^{+0.6}_{-0.5}$	10^{+3}_{-2}	Velocity dispersion	15.69 ± 0.01	1.79 ± 0.01	0.81
SpARCS J104737+574137	0.956	$0.29^{+0.10}_{-0.13}$	$1.00^{+0.40}_{-0.49}$	Velocity dispersion	17.14 ± 0.03	1.89 ± 0.03	0.24
SpARCS J021524−034331	1.004	$0.26^{+0.17}_{-0.13}$	$1.0^{+0.8}_{-0.5}$	Velocity dispersion	16.88 ± 0.14	1.86 ± 0.05	0.33
SpARCS J105111+581803	1.035	$0.12^{+0.03}_{-0.06}$	$0.42^{+0.12}_{-0.23}$	Velocity dispersion	16.88 ± 0.05	1.74 ± 0.03	0.35
SpARCS J161641+554513	1.156	$0.28^{+0.11}_{-0.12}$	$1.3^{+0.6}_{-0.6}$	Velocity dispersion	17.02 ± 0.03	1.73 ± 0.02	0.36
SpARCS J163435+402151	1.177	$0.44^{+0.11}_{-0.16}$	$2.1^{+0.6}_{-0.9}$	Velocity dispersion	17.35 ± 0.02	1.84 ± 0.03	0.27
SpARCS J163852+403843	1.196	$0.10^{+0.03}_{-0.05}$	$0.38^{+0.15}_{-0.21}$	Velocity dispersion	17.65 ± 0.05	1.91 ± 0.05	0.21
SpARCS J003550−431224	1.340	$0.39^{+0.13}_{-0.15}$	$2.5^{+1.0}_{-1.1}$	Velocity dispersion	17.52 ± 0.01	1.98 ± 0.01	0.29
SpARCS J033056−284300	1.620	$0.24^{+0.10}_{-0.15}$	$2.1^{+1.1}_{-1.4}$	Velocity dispersion	17.88 ± 0.04	...	0.29
SpARCS J022426−032331	1.630	$0.04^{+0.01}_{-0.03}$	$0.26^{+0.05}_{-0.17}$	Velocity dispersion	18.07 ± 0.03	...	0.25
CL J0152.7−1357	0.830	$0.45^{+0.17}_{-0.14}$	$1.4^{+0.6}_{-0.5}$	X-ray temperature	16.96 ± 0.08	1.80 ± 0.08	0.23
XLSS J022303.0−043622	1.220	$0.15^{+0.04}_{-0.03}$	$0.68^{+0.20}_{-0.17}$	X-ray temperature	17.72 ± 0.01	1.82 ± 0.01	0.21
XLSS J022400.5−032526	0.810	$0.19^{+0.05}_{-0.04}$	$0.56^{+0.15}_{-0.13}$	X-ray temperature	16.49 ± 0.10	...	0.34
RCS J0439−2904	0.950	$0.03^{+0.01}_{-0.01}$	$0.08^{+0.04}_{-0.02}$	X-ray temperature	17.70 ± 0.08	1.86 ± 0.08	0.14
2XMM J083026+524133	0.990	$0.98^{+0.24}_{-0.21}$	$4.0^{+1.1}_{-1.0}$	X-ray temperature	16.58 ± 0.05	1.90 ± 0.06	0.43
RX J0848.9+4452	1.260	$0.47^{+0.17}_{-0.13}$	$2.7^{+1.2}_{-0.8}$	X-ray temperature	17.00 ± 0.02	1.86	0.42
RDCS J0910+5422	1.110	$0.55^{+0.30}_{-0.19}$	$2.7^{+1.8}_{-1.1}$	X-ray temperature	17.88 ± 0.05	1.83 ± 0.06	0.15
CL J1008.7+5342	0.870	$0.19^{+0.10}_{-0.06}$	$0.54^{+0.32}_{-0.19}$	X-ray temperature	16.42 ± 0.08	1.97 ± 0.09	0.41
RX J1053.7+5735 West	1.140	$0.25^{+0.04}_{-0.03}$	$1.1^{+0.2}_{-0.2}$	X-ray temperature	17.21 ± 0.06	1.99 ± 0.07	0.29
MS1054.4−0321	0.820	$0.97^{+0.28}_{-0.22}$	$3.4^{+1.1}_{-0.8}$	X-ray temperature	16.04 ± 0.10	1.80 ± 0.10	0.53

© 2012 The Authors, MNRAS **427,** 550–568
Monthly Notices of the Royal Astronomical Society © 2012 RAS

Table A3 – *continued*

Name	Redshift	Cluster Mass (10^{15} M$_\odot$)	Cluster Mass today (10^{15} M$_\odot$)	Mass proxy	BCG K_s (mag)	BCG $J-K_s$ (mag)	BCG Stellar mass (10^{12} M$_\odot$)
CL J1226+3332	0.890	$1.8^{+0.4}_{-0.4}$	$6.6^{+1.7}_{-1.5}$	X-ray temperature	16.00 ± 0.06	1.71 ± 0.07	0.63
RDCS J1252.9−2927	1.240	$0.66^{+0.08}_{-0.11}$	$3.9^{+0.6}_{-0.7}$	X-ray temperature	17.36 ± 0.03	1.83 ± 0.01	0.30
RDCS J1317+2911	0.810	$0.24^{+0.19}_{-0.09}$	$0.71^{+0.66}_{-0.29}$	X-ray temperature	17.27 ± 0.15	1.68 ± 0.17	0.17
WARPS J1415.1+3612	1.030	$0.54^{+0.15}_{-0.12}$	$2.3^{+0.8}_{-0.6}$	X-ray temperature	16.76 ± 0.04	1.86 ± 0.05	0.39
CL J1429.0+4241	0.920	$0.57^{+0.32}_{-0.17}$	$2.1^{+1.4}_{-0.7}$	X-ray temperature	17.43 ± 0.20	1.78 ± 0.22	0.18
CL J1559.1+6353	0.850	$0.25^{+0.21}_{-0.11}$	$0.74^{+0.72}_{-0.35}$	X-ray temperature	17.21 ± 0.09	1.90 ± 0.12	0.19
CL1604+4304	0.900	$0.09^{+0.10}_{-0.04}$	$0.23^{+0.30}_{-0.12}$	X-ray temperature	17.61 ± 0.09	1.68 ± 0.12	0.15
RCS J162009+2929.4	0.870	$0.31^{+0.37}_{-0.14}$	$0.95^{+1.33}_{-0.45}$	X-ray temperature	17.63 ± 0.12	...	0.14
XMMXCS J2215.9−1738	1.460	$0.18^{+0.06}_{-0.07}$	$1.1^{+0.5}_{-0.5}$	X-ray temperature	18.72 ± 0.01	1.84 ± 0.02	0.11
XMMU J2235.3−2557	1.390	$0.88^{+0.30}_{-0.24}$	$6.5^{+2.7}_{-2.0}$	X-ray temperature	17.34 ± 0.01	1.87 ± 0.02	0.37

Table A4. BCGs without cluster mass measurements.

Name	Redshift	K_s (mag)	$J-K_s$ (mag)	Stellar mass (10^{12} M$_\odot$)
Abell 2292	0.119	12.06	1.06	0.59
Abell 2665	0.056	10.74	1.11	0.47
Abell 291	0.196	14.10	1.32	0.22
MACS J0150.3−1005	0.363	13.90	...	0.82
MACS J0329.6−0211	0.451	14.13	...	1.07
MACS J1359.8+6231	0.330	14.32	...	0.45
MACS J2050.7+0123	0.333	14.67	...	0.33
MACS J2214.9−1359	0.495	14.71	1.67	0.76
MACS J2241.8+1732	0.317	14.39	...	0.39
RCS0224−0002	0.770	16.87	...	0.22

This paper has been typeset from a TEX/LATEX file prepared by the author.